

**Direct Waveform Inversion Using Explicit Time-Space Causality Principle**

by  
Zhonghan Liu

A dissertation submitted to the Department of Earth and Atmospheric Sciences,  
College of Natural Sciences and Mathematics  
in partial fulfillment of the requirements for the degree of

DOCTOR OF PHILOSOPHY

in Geophysics

Chair of Committee: Hua-Wei Zhou

Committee Member: Yingcai Zheng

Committee Member: Shuhab Khan

Committee Member: Jonathan Liu

University of Houston

May 2021

Copyright 2021, Zhonghan Liu

## **Acknowledgments**

I would like to express my deep and sincere gratitude to my research advisor and the chairman of my dissertation committee, Prof. Hua-Wei Zhou. He has provided me the opportunity to pursue the Ph.D. degree in geophysics and has taught me a broad spectrum of necessary geophysical concepts and methods to build a solid background for my research. He has also kindly provided me much guidance and support every time I came across difficulties in my life. Without his guidance and support, this dissertation would not have been possible.

I am also extremely grateful to my co-advisor and the member of my dissertation committee, Prof. Yingcai Zheng, for encouraging me to pursue the Direct Waveform Inversion idea and providing me guidance all along my Ph.D. study. He has not only taught me the methodologies to carry out the research but also helped me greatly improve my technical writing and communication skills. He also generously offered me research assistantships, which resolved my financial burden. It is a great privilege and honor to work and study with him.

I would like to show my great appreciation to Prof. Shuhab Khan, who served as a member of my dissertation committee. He has provided many precious suggestions and guidance on the format of my dissertation. In addition, as the

department graduate advisor, he has been patiently helping me with questions regarding the departmental policies and rules since the beginning of my Ph.D. study.

I am indebted to Dr. Jonathan Liu, who served as the external member of my dissertation committee. Dr. Liu is always very supportive and responsive. He took his valuable time and provided me many helpful suggestions based on his profound experiences.

I would also like to show my great appreciation to Prof. Donald Kouri, who formerly served as a member of my dissertation committee. He has provided me many helpful thoughts back on my Ph.D. dissertation proposal. In addition, his inverse scattering theory course introduced me to a brand-new aspect to understand the wave propagation theories and benefited my research a lot. Unfortunately, Dr. Kouri passed away early this year. My interactions with him will be greatly missed.

I would also like to extend my greatest appreciation to my colleagues and friends in the EAS department of the University of Houston. Dr. Hao Hu provided me with many constructive discussions on my research and helped me a lot in revising my dissertation. Dr. Yang Mu and Dr. Yukai Wo helped me in many aspects of my life.

Finally, I would like to thank the emotional support and encouragement from my family. Without their help, my work would not have been completed.

In my dissertation, Chapter 2 is from my publication in the journal *Communications in Computational Physics* (Zheng and Liu 2020). Chapter 3 and

Chapter 4 are based on two of my manuscripts to be submitted. I appreciate the contributions and help from Prof. Yingcai Zheng, Prof Hua-Wei Zhou, and Dr. Hao Hu.

## **Abstract**

I propose a Direct Waveform Inversion (DWI) scheme to address several existing challenges in many full waveform inversion (FWI) methods. A key ingredient in DWI is the explicit use of the wavefield time-space causality property in the inversion, which allows us to convert the global non-linear optimization problem in the FWI, into local linear inversions that can be readily solved. DWI is a recursive scheme that sequentially inverts the subsurface model in a shallow-to-deep fashion. Therefore, there is no need for a global initial velocity model to implement DWI and the DWI is unconditionally convergent. For DWI to work, DWI must use the full seismic wavefield, including internal and free-surface multiples, and it combines seismic migration and velocity model inversion into one single process. Therefore, DWI simultaneously obtains interface information and the interval velocities.

In this dissertation, I first illustrate the basic idea of DWI in 1D horizontally layered models with plane wave incidence using numerical examples. The basic idea is to build a recursive scheme by decomposing and extrapolating wavefields in each layer and applying the localized inversion to find the properties of the next layer. I apply the DWI concept to several scenarios, including inversion of both P-wave velocity and density in the 1D stratified layered model using both plane wave and point source incidence, inversion of a 2D model using a point source. For the simultaneous inversion of velocity and density structure, I use the angle-dependent reflections from multiple plane wave sources to improve the stability of the inversion. To invert for the 2D model with point sources, I use the boundary integrals to

decompose and extrapolate the spherical waves, during the process I use a localized reverse time migration (RTM) method to look ahead to locate the next layer. For the inversion of the 1D stratified layered model with a point source, I develop a new 1D scheme for the spherical wave case. Numerical examples are presented for all these different scenarios. In the final part, I review applications of the Gelfand-Levitan-Marchenko (GLM) equation in geophysics studies and discuss their relations to my DWI.

# TABLE OF CONTENTS

Acknowledgments.....	iii
Abstract.....	vi
TABLE OF CONTENTS.....	viii
List of Figures .....	x
Chapter 1. Introduction .....	1
1.1 Review of seismic waveform inversion.....	1
1.2 Overview of the dissertation chapters.....	5
Chapter 2. Direct Waveform Inversion in the 1D stratified layered acoustic medium with plane wave incidence	8
2.1 Introduction .....	8
2.2 Basic idea of the DWI .....	12
2.3 Two synthetic examples.....	16
2.4 Discussions.....	20
2.5 Conclusions .....	21
Chapter 3. DWI for density and velocity simultaneously in a 1D stratified layered acoustic medium with plane wave incidence.....	23
3.1 Introduction .....	23
3.2 Inverting model's velocity and density using the DWI scheme .....	25
3.3 Numerical Examples.....	27
Example 1.....	28
Example 2.....	34
3.4 Conclusion and discussions.....	41
Chapter 4. DWI for velocity in the 2D irregular bounded layered acoustic medium with point source	43
4.1 Introduction .....	43
4.2 Inverting model's velocity using the 2D DWI scheme .....	46
4.2.1 Separate & Extrapolate wavefields in a layered medium.....	46
4.2.2 Decompose & extrapolate the wavefields in a 2D layered model .....	47
4.2.3 Detect the lower boundary & apply the localized inversion .....	50
4.3 Numerical examples.....	52

4.4	Discussions .....	60
4.5	Conclusions .....	61
Chapter 5.	DWI for velocity inversion in a 1D stratified layered acoustic medium with point sources 63	
5.1	Introduction .....	63
5.2	Applying the modified 1D DWI scheme in 1D stratified layers with point source .....	64
5.2.1	Applying 1D scheme on 2D data to invert for the current layer's thickness .....	66
5.2.2	Applying 1D scheme on 2D data to invert for next layer's velocity .....	68
5.3	Numerical example .....	70
5.4	Discussion and Conclusions .....	76
Chapter 6.	Relation to the Gelfand-Levitan-Marchenko (GLM) Equation in Geophysical Study .....	77
6.1	Introduction .....	77
6.2	Review of the application of the GLM equation in geophysics studies .....	79
6.2.1	Applying the GLM equation for the 1D direct inversion .....	79
6.2.2	Applying the GLM equation in the 1D focusing approaches .....	81
6.3	Numerical test.....	85
6.4	Discussions .....	90
6.5	Conclusions .....	91
Bibliography	.....	92

## List of Figures

<b>Figure 2.1:</b> DWI process for a 1D layered model. ....	13
<b>Figure 2.2:</b> True model (red line) VS the DWI inverted model (black line).....	17
<b>Figure 2.3:</b> The down-going (a) and up-going (b) wavefields calculated from the record. Note the red part in the down-going time series is amplified by ten times.....	18
<b>Figure 2.4:</b> Comparison between the true model(red line) and the DWI inversion result(blue line).....	19
<b>Figure 2.5:</b> The down-going (a) and up-going (b) wavefields calculated from the record. Note the red part in the down-going time series is amplified by ten times.....	20
<b>Figure 3.1:</b> Velocity (a) and density (b) profiles of the true model.....	29
<b>Figure 3.2:</b> Recorded wavefields of pressure (a)-(d) and vertical component of particle velocity (e)-(h) in response to four different plane waves. The amplitudes in red dashed frames are amplified by 300 times. ....	30
<b>Figure 3.3:</b> Comparisons between the DWI inversion result and true model on velocity (a) and density (b) models. ....	31
<b>Figure 3.4:</b> Comparisons of data (red) and synthetics (black) modeled using the DWI inverted model for pressure (a) and particle velocity (b) at the 0-degree incidence. Note the waveform amplitudes in the red dashed box are amplified by 300 times.....	33
<b>Figure 3.5:</b> The velocity (a) and density (b) profiles of the true model for the DWI.....	35
<b>Figure 3.6:</b> Recorded wavefields of pressure (a)-(d) and vertical component of particle velocity (e)-(h) in response to four different plane waves. The events in red dashed frames are amplified by 10 times. ....	36
<b>Figure 3.7:</b> Comparisons between the DWI inverted model and true model on velocity (a), density (b) and impedance (c) models. ....	39
<b>Figure 3.8:</b> Comparisons of data (red) and synthetics (black) modeled using the DWI inverted model for pressure at the 0-degree incidence (a), the events in the red dashed box are amplified by 10 times. A zoomed in view of the events in the red dashed box are presented in (b).....	40
<b>Figure 4.1:</b> Wavefields in a 2D layered model. $c_0, c_1, c_2$ are the velocities of each layer. The whole model has a uniform density value $\rho$ . ....	46
<b>Figure 4.2:</b> Velocity profile of the true model. ....	53
<b>Figure 4.3:</b> (a) The pressure field at layer 2's top. (b) The particle velocity field at layer 2's top. Events in red are amplified by 300 times.....	54
<b>Figure 4.4:</b> (a) The up-going pressure field at layer 2's top. (b) The down-going pressure field at layer 2's top. Events in red are amplified by 300 times.....	55
<b>Figure 4.5:</b> Migrated image by using a half space with constant layer 2's velocity as model and decomposed up-going and down-going pressure fields as input. ....	56
<b>Figure 4.6:</b> (a) The up-going and down-going pressure fields at point right on layer 2's lower boundary. (b) The up-going and down-going pressure fields at point one grid above layer 2's lower boundary. ....	57
<b>Figure 4.7:</b> (a) Deconvolution results from the up-going and down-going pressure fields at point right on layer 2's lower boundary. (b) Deconvolution results from the up-going and down-going pressure fields at point one grid above layer 2's bottom boundary. ....	58
<b>Figure 4.8:</b> (a): The pressure wavefield at layer 2's bottom. (b): The particle velocity wavefield at layer 2's bottom. Events in red were amplified by 15 times.....	58
<b>Figure 4.9:</b> (a) The original velocity model (b) The inverted velocity model.....	59

<b>Figure 4.10:</b> Gather of input pressure wavefield (a) versus gather of modeled pressure wavefield(b) from inversion result.....	60
<b>Figure 5.1:</b> Wavefields in a 2D stratified layered model. The whole model has a uniform density value $\rho$ . .....	65
<b>Figure 5.2:</b> Velocity profile used for generating synthetic data .....	71
<b>Figure 5.3:</b> Pressure(a) and particle velocity(b) fields record used for the inversion. ....	72
<b>Figure 5.4:</b> Comparison of the up-going pressure fields calculated at the receiver depth using the velocity profile in Figure 5.2 with a point source (blue) and plane wave incidence (red).....	73
<b>Figure 5.5:</b> Result before(a) and after(b) removal of the errors at the third layer's top. ....	74
<b>Figure 5.6:</b> Comparison between the inversion result (red) and input velocity profile (blue). ....	75
<b>Figure 6.1:</b> A step-function velocity profile, the velocity is $c_0$ to the left of $x_s$ and $c_1$ to the right of $x_s$ . $R$ is the reflection coefficient and $T$ is the transmission coefficient. The horizontal arrows show the direction of events' propagation. (a) The reflected and transmitted pulses due to the delta function. (b) The incident fields focus at $x_f$ , consist of two pulses with strength one and a second impulse with strength $-R$ . (c) The fields focus at $x_f$ , the reflected pulse is cancelled by the second incident pulse.....	82
<b>Figure 6.2:</b> Velocity profile of the true model. The velocity is generated by the tapered cosine function.	86
<b>Figure 6.3:</b> Deconvolved Data as 1D inversion's input. ....	86
<b>Figure 6.4:</b> The diagonal terms $Kdiag$ of the kernel function matrix $K$ after the first iteration (red line), third iteration (blue line), and fifth iteration (black line). ....	87
<b>Figure 6.5:</b> Time series of scattering potential $q$ calculated from the true model and $Kdiag$ . ....	88
<b>Figure 6.6:</b> Comparison of the Inversion results calculated from $q$ , $K$ and the true model. ....	89

## **Chapter 1. Introduction**

### **1.1 Review of seismic waveform inversion**

Seismic waveform inversion is an important tool for mapping and understanding the subsurface property in both exploration and global seismology. There are several different research directions for waveform inversion. Among them, the Full Waveform Inversion (FWI) methods are the most well developed and have already become a conventional processing step in geophysics studies. In the early 1980s, Lailly (1983) and Tarantola (1984) firstly proposed the idea of the FWI based on the single scattering Born approximation: the FWI converts the non-linear seismic waveform inversion into a linear problem by matching waveform information between seismic records and modeled dataset based on an initial model to iteratively update the model. The goal is to find a final model which is consistent with the observed data. In recent decades, FWI was extensively discussed and developed, including inverting for more complicated media and more parameters (Tarantola 1986, Pratt 1999, Pratt and Shipp 1999, Virieux and Operto 2009). Using global matching and the Born approximation features, FWI heavily relies on the low-wavenumber information from the starting model and low-frequency information from the dataset. Unfortunately, these two pre-requisites are very difficult to achieve in real seismic surveys, as the subsurface geological structure is always very complex, and the seismic data are bandlimited (i.e., lacking of frequency content  $< 5$  Hz). Moreover, the perturbation approach in FWI demands for significant computational

resources. To alleviate these challenges, lots of work have been done from different aspects. Examples include the Laplace FWI (Shin and Cha 2008, Shin and Ha 2008, Kim et al. 2013), envelope inversion (Wu et al. 2014, Luo and Wu 2015, Chen et al. 2018), intensity inversion (Liu et al. 2018, Liu et al. 2020), and the FWI using deep learning techniques (Richardson 2018).

Besides the FWI methods that invert the model through a global fitting approach, direct inversion methods also play a significant role in the seismic waveform inversion study. The idea of the direct inversion firstly comes from the inverse scattering problems, aiming to determine a target's characteristics from its scattered field. Ware and Aki (1969) begun the study of direct non-linear waveform inversion in the 1D medium. They first established the relationships between scattering potentials and recorded responses by representing the wave equations using the Schrodinger equation, then applied the Gelfand-Levitan-Marchenko (GLM) scheme (Agranovich and Marchenko 2020). Without any *a priori* knowledge of the model, the GLM scheme can determine the model's potential directly from the response. However, by representing the wave equation using the Schrodinger equation, a second derivative operator is applied to the impedance function, making the scheme almost only applicable to continuous medium for a typical seismic frequency bandwidth.

In 1997, Weglein and his colleagues extended some early works (Moses 1956, Razavy 1975) and developed the inverse scattering method (Weglein et al. 1997, Weglein et al. 2000, Weglein et al. 2001, Weglein et al. 2003). The inverse scattering

method is a direct non-linear inversion with the advantage of not requiring prior knowledge of an initial velocity model. However, the convergence of the entire series can be a problem for large scale strong-contrast objects (Prosser 1969, Prosser 1976, Prosser 1980, Prosser 1982, Weglein et al. 1997). To solve the convergence problem, Weglein and his colleagues introduced the concept of “subseries”. The subseries, isolated from the whole scattering series according to different tasks, could converge. On the other hand, Yao et al. (2014) proposed another direct non-linear inversion scheme using the Volterra inverse scattering series. Based on the previous work from Sams and Kouri (1969), the convergence behavior of the Volterra series is guaranteed in the forward modeling. However, the inverse scattering series (ISS) using the Volterra series still suffers a convergence problem. Eftekhari et al. (2018) introduced the Shanks transform and achieved convergence acceleration for strong-contrast media.

The research interest of the GLM scheme was renewed by Rose (2002) and gained momentum recently. He presented a focusing approach that allows one to focus the wavefield to any point in a 1D space by constructing an incident wavefield using a delta function and time-reversed solution of the GLM scheme. Later on, Rose’s approach got further extended and developed into the Marchenko method by Slob et al. (2014), Wapenaar et al. (2014), and Wapenaar et al. (2014). Unlike the traditional seismic interferometry approaches, the Marchenko method can generate the seismic response from the source at the surface to any point into the model and determine the Green’s function beneath the focusing depth simultaneously using the

only surface recorded dataset while a reference background velocity model between the surface and the focus depth is available. By retrieving the focused wavefields and Green's function indirectly, the Marchenko method provides a novel target-oriented solution for both imaging and inversion schemes aiming at areas beneath complex structures.

In 2015 Liu and Zheng (2015) proposed a new direct inversion scheme called the Direct Waveform Inversion (DWI) to invert for the model's velocities and layering simultaneously in a 1D medium. Instead of either the GLM scheme or the Born-Neumann series, a different route was pursued by Liu and Zheng, exploiting the space-time causality of the wavefield. In the DWI scheme, a global non-linear inversion problem is converted into many local inversions using a recursive process in a shallow to deep fashion. In each recursion step, the up-going and down-going wavefields are decomposed at the top of the layer and then extrapolated to the bottom of the layer. Following a linear inversion, the next (deeper) layer's property could be determined directly from the extrapolated wavefields. Based on a similar idea, I further proposed two different DWI schemes: inverting for velocities and geometries in a 2D irregular layered medium using point sources, and inverting for velocities, densities, and geometries for the 1D case using point sources. Results from the numerical modeling demonstrate that DWI has a great potential in inverting waveforms in more complex scenarios.

## 1.2 Overview of the dissertation chapters

This dissertation presents the DWI details and its implementation in different scenarios. As a very different framework from other waveform inversions, DWI conducts inversion recursively, according to the causality rule. It provides a great potential for processing the seismic dataset more efficiently, capable to tackle some persisting problems in the conventional waveform inversion studies.

In Chapter 2, I apply the DWI scheme in a 1D stratified layered model with a uniform density value through the whole model. The dataset is generated from a normal incident plane wave. Here I use the a 1D case to demonstrate the basic idea of the DWI scheme and its workflow, which also serves as the fundamental framework for all subsequent cases. Two synthetic tests are shown to validate this method under different conditions, including the free surface effect, strong velocity contrasts, and thin layer effects.

In Chapter 3, I investigate and expand the DWI scheme for the 1D multi-parameter inversion cases. In this study, the 1D model is still composed of horizontally stratified layers of variable densities in layers. The influences of velocity and density on the wavefield are always entangled together. It brings extra difficulties in performing the multi-parameter inversion. Using multiple plane waves at different incident angles, I developed a new 1D DWI scheme for simultaneously inverting the

layer depth, velocity, and density. Two synthetic tests are provided. The test result shows the DWI is able to perform the multi-parameter inversion.

In Chapter 4, I extend the DWI scheme to a 2D layered model. In this study, the layer geometries are no longer constrained as horizontally stratified boundaries. The seismic dataset is generated by a point source. For the 2D case, I upgrade the wave propagation kernel using the boundary element method and use the conventional RTM and raytracing approach to handle the non-uniqueness issue of the 2D ray paths. At the end of this study, a synthetic example is shown, in which the model has strong velocity variations and irregular boundaries of the layers. The inversion result proves the feasibility of the 2D DWI scheme.

In Chapter 5, I will go back to the 1D DWI scheme. Unlike the previous 1D studies in Chapter 2, I modify the 1D DWI scheme to be applicable for the zero offset dataset from a 1D stratified layered medium with a point source. Since the 1D wave propagator can get amplitude errors in the point source case, only traveltime information is utilized in most parts of this scheme to avoid this issue. Moreover, two forward modeling process are introduced based on the inverted model help to retrieve the velocities and layer depths. A synthetic test is made to show the accuracy of this modified 1D DWI scheme.

In Chapter 6, I will review the GLM equation related methods. As an important equation governs a significant part of the inverse theory, this equation was first applied to the seismic waveform inversion in the 1960s and the interest has been revived in the early 2000s for wavefield focusing study, and still is an active research. Some features in GLM are similar with the DWI schemes. However, DWI is a more powerful method than GLM as we will see. The review covers both early applications of GLM in seismic waveform inversion and recent focusing approaches. At the end of this review, there will be a discussion comparing the GLM equation method and the DWI methods.

## **Chapter 2. Direct Waveform Inversion in the 1D stratified layered acoustic medium with plane wave incidence**

In this Chapter, I present the basic idea of the Direct Waveform Inversion (DWI) using a 1D stratified layered acoustic model and demonstrate its application with numerical examples.

### **2.1 Introduction**

The seismic full waveform inversion (FWI) (Lailly 1983, Tarantola 1984) initially formulated in the time domain represents an important conceptual leap whose purpose is to find a subsurface model that can be used to predict observed seismic waveforms in both phase and amplitude, wiggle to wiggle. The FWI can also be implemented in the frequency domain (Liao and McMechan 1996, Pratt 1999, Pratt and Shipp 1999, Sirgue and Pratt 2004). Despite some success, the FWI mathematical formulation has significant physical limitations. This chapter aims to propose a new formulation, called direct waveform inversion (DWI), to overcome these limitations. At present, the DWI is by no means perfect, but it provides promising directions for waveform inversion.

The seismic FWI problem was frequently cast into a global nonlinear mathematical optimization problem. A model is sought to minimize a misfit/objective function defined between the observed data and the model-predicted data (Virieux and Operto 2009). The nonlinearity arises because the change in seismic data in

response to the change in the model parameter is not linear. In FWI, one linearizes the problem around a starting model and then computes the local gradient (e.g., the Frechet derivative) of the data perturbation with respect to the model perturbation and updates the model along the gradient direction. The updated model will be the next starting model, and this process can be iterated until a certain convergence criterion about the misfit is met.

Challenges to implementing the FWI were almost immediately recognized since the inception of the FWI idea (Lailly 1983, Tarantola 1984). The first one is the initial-model dependence and convergence issue in the nonlinear global optimization. The second one is the FWI's apparent lack of ability to recover low-wavenumber (large-scale) strong-contrast model variations.

The FWI results strongly depend on the initial model that is usually not an outcome of the FWI itself but is provided as an input to the FWI. The FWI works well if a good initial model in the neighborhood of the true model can be found at the beginning (Gauthier et al. 1986, Tarantola 1986, Mora 1987, Bourgeois et al. 1989). Suppose the initial model is far from the true model. In that case, the FWI iteration may converge to a local minimum of the objective function, and the global optimization cannot be attainable. Real geological models are likely to be complicated. Demanding an initial model that is already close to the true model undercuts the true value of the practical implementation of the FWI. Fortunately, Kolb et al. (1986) showed in numerical examples that if a coarsely smoothed version of the true model is available as the starting model, the FWI could converge to the

true model. This conclusion had been confirmed more recently (Sirgue and Pratt 2004, Pratt 2008). Can the FWI produce its own low wavenumber initial modeling? Within the gradient-based FWI theoretical framework, the low frequency seismic data is needed in order for the FWI to recover the low-wavenumber model component (Kolb et al. 1986, Bunks et al. 1995) because the FWI formulation/approximation is more linear/accurate at low frequencies. Seismic data in exploration settings are bandlimited. However, even without the low frequency data, the low-wavenumber model information is indeed contained in the data. It can be readily obtained using many other methods such as traveltimes tomography or the normal moveout analysis (Mora 1989). The inability of FWI to invert for low wavenumber model variations relative to a simple starting model (e.g., homogeneous or linear) shows the deficiency in the FWI formulation.

The gradient-based FWI methods do not account for the full physics of wave scattering and propagation. Tarantola (2005, p.128) pointed out that the FWI local Frechet gradient amounts to the linear single scattering Born approximation. Recent work by Wu and Zheng (2014) showed a one-to-one correspondence between the  $n^{th}$  order Frechet derivative and the  $n^{th}$  order multiple Born scattering. This means that FWI's dropping high order functional derivatives is to physically ignore possible multiple scattering among unknown model perturbations/scatterers. This is a significant drawback in the FWI assumption. Wu and Zheng (2014) further showed in numerical modeling that including multiple forward scattering is critical to building

correct traveltimes for transmission paths. Both transmitted and reflected waves have transmission paths. Therefore, it is to be able to take into account multiple scattering among model perturbations in waveform inversion. (Note that the single scattering here is referred to single interactions between the background wavefield with the unknown model perturbations. However, the background field can be multiply scattered by structure contained in the background model.) The Born approximation is accurate if the following two conditions are satisfied: the data frequency is low or if the perturbation size is small compared to the wavelength, and the unknown model perturbation is weak. The first condition can be fulfilled if the starting model's low-wavenumber component matches the true model's low-wavenumber component.

Within the FWI theoretical framework, there has been a significant amount of work to obtain a low-wavenumber initial model, which is then used as an input to the FWI in the sequel. This includes the envelope inversion (Bozdağ et al. 2011, Wu et al. 2013, Wu et al. 2014, Luo and Wu 2015, Chen et al. 2018, Wang et al. 2018), intensity inversion (Liu et al. 2018), waveform correlation function inversion (Van Leeuwen and Mulder 2008), and the Laplace FWI (Ha and Shin 2013) and so on. There are also efforts to extrapolate the bandwidth of the data to ultra-low frequency (Xie 2013, Li and Demanet 2016).

Recently, Liu and Zheng (Liu and Zheng 2015, Liu and Zheng 2017) proposed a reflection direct waveform inversion (DWI) scheme by explicitly exploiting the causality of space-time wavefield in the inversion process as a constraint. As a result, the DWI converts a global nonlinear problem into many local linear inversion

problems. The DWI does not require an initial global model. DWI first inverts for the shallow model and then recursively inverts for the deeper model. Unlike the FWI iterative process, this recursion process is always convergent, and in the meantime, it can fit the waveforms. DWI must use all wave types (primary reflections, internal and free surface multiples, etc.). DWI represents a different theoretical framework compared to gradient-based inversion methods. My focus here is to expand and review the basic ideas of DWI using the time-space causality principle as an explicit constraint so that this idea can be developed further by interested people.

## 2.2 Basic idea of the DWI

The explicit use of the time-space causality concept in DWI can be simply understood in a 1D case along the  $z$ -direction (Figure 2.1). The model can be parameterized as a stack of horizontally stratified layers. Consider the acoustic case, each layer is homogeneous and characterized by a sound speed,  $c_i$ , and a layer thickness,  $H_i$ , where the subscript indicates the layer number (Figure 2.1). The pressure field is  $P(z,t)$ , and the particle velocity field is  $V_z(z,t)$ , where  $z$  is the depth, and  $t$  is time.  $U(z,t)$  and  $D(z,t)$  are up-going and down-going pressure fields at  $z$ , respectively. To simplify notations, I use  $P_i = P_i(z_i, t)$ ,  $V_{zi} = V_z(z_i, t)$ ,  $D_i^\pm = D_i(z_i^\pm, t)$ , and  $U_i^\pm = U_i(z_i^\pm, t)$ .  $z_i^+$  and  $z_i^-$  represent depths slightly below and above  $z_i$ , respectively.

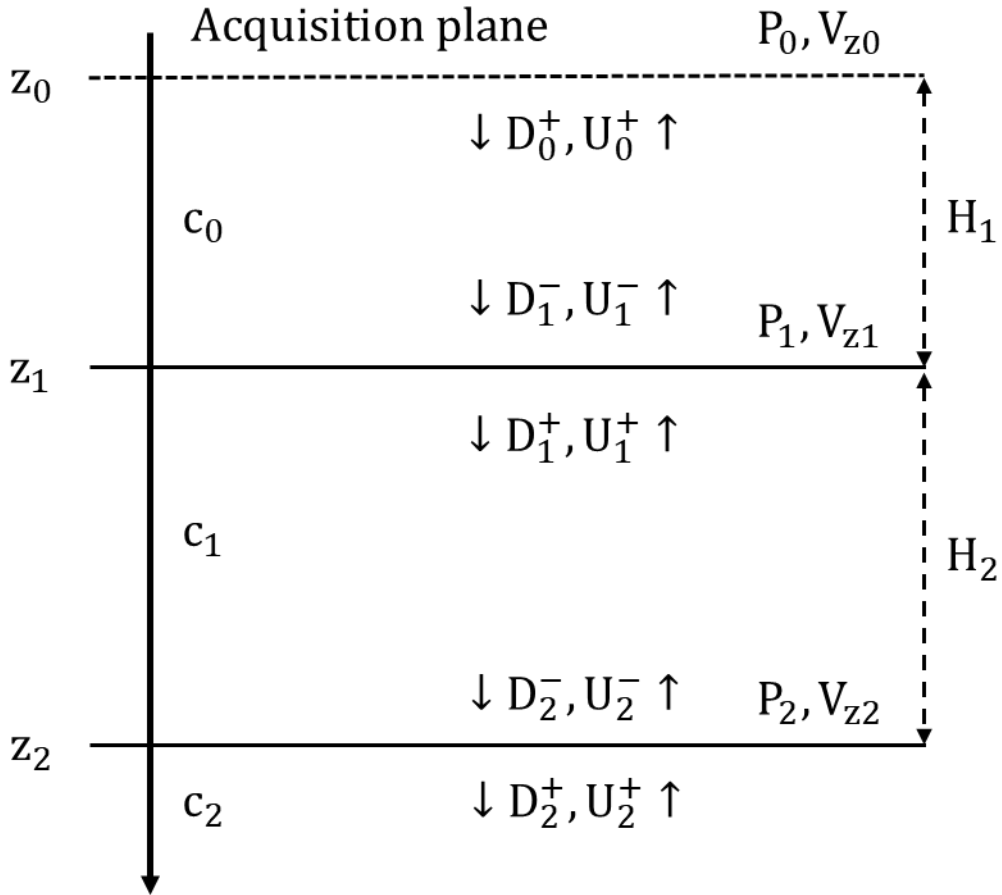


Figure 2.1: DWI process for a 1D layered model.

The starting assumptions are:

- (i) The incident wave is a down-going plane wave initiated at time zero at the acquisition-plane  $z_0$ . The wavelet is an impulse.
- (ii) Both the wave pressure  $P_0$  and the vertical particle velocity  $V_{z0}$  are recorded. The recorded waves include all the primary reflections, as well as the multiple reflections among all layers.
- (iii) The model parameters for all layers are unknown except the velocity of the

top layer is known,  $c_0$ .

(iv) All layers have the same density,  $\rho_i = \rho$ .

Having both types of data (pressure and particle velocity) will allow us to separate the wavefield at a depth into up-going and down-going waves (Backus (1959)). In many cases, only one type of data is available. If only pressure data are available, we can predict the particle velocity data (Amundsen 1993, Amundsen et al. 1995, Zheng 2010). Because I assume the availability of both pressure and particle velocity data, it does not matter whether the acquisition plane is a free surface or not. For now, the first layer is regarded as an infinite half space.

For plane waves, I can decompose the pressure–velocity data,  $P-V_z$ , at a depth level into an up-going  $U$  and a down-going  $D$  pressure wave at the same depth via the following two relations:

$$P = D + U, \tag{2.1}$$

$$I \cdot V_z = D - U, \tag{2.2}$$

where  $I$  is the acoustic impedance, defined as the product of sound speed and density.

Now the DWI inversion steps are described as follows:

- (1) Using the recorded data,  $P_0$  and  $V_{z0}$ , I can obtain the up-going and down-going pressure at  $z_0$ ,  $U_0^+$  and  $D_0^+$ , respectively;
- (2) If there is no free surface, there will be only one pulse in  $D_0^+(t)$  which is the direct wave at time zero. However, the up-going wave  $U_0^+(t)$  may have many arrivals due to wave interaction with multiple layer interfaces. It is known that

the earliest arrival in  $U_0^+(t)$  must be from the nearest reflector, which is at  $z_1$ .

I can undoubtedly pick its traveltime,  $t_1$  and amplitude,  $A_1$ . Reflections from any other depths must come later than  $t_1$  and this is the time-space causality principle which states a correspondence between the earliest arrival in time and the nearest reflector in space;

- (3) Since I know  $c_0$  and have picked  $t_1$ , I can compute the distance  $H_1$  to obtain the depth of the first reflector  $z_1$ :  $H_1 = c_0 t_1 / 2$  and  $z_1 = z_0 + H_1$ .
- (4) I extrapolate the up-going and down-going pressure wavefields from  $z_0$  to depth  $z_1^-$  and get  $U_1^-$  and  $D_1^-$ .  $D_1^-$  is a time-delayed version of  $D_0^+$  and the amount of time delay is  $H_1 / c_0$ . On the other hand,  $U_1^-$  is a time-advanced version of which means I need to shift  $U_0^+$  to the negative time direction to get  $U_1^-$  and the amount of time shift is  $-H_1 / c_0$ . The amplitude ratio  $A_1 = U_1^-(t_1) / D_1^-(t_1)$  is related to the impedance contrast between the two layers:  $A_1 = (c_1 - c_0) / (c_1 + c_0)$  so I can obtain the velocity  $c_1$  for the next layer;
- (5) From  $U_1^-$  and  $D_1^-$  and using Equation (2.1), I can obtain the  $P-V_z$  data at depth  $z_1^-$ ,  $P_1$  and  $V_{z1}$ . The  $P-V_z$  data are continuous across the boundary so I can pass the  $P-V_z$  data to depth  $z_1^+$ ;
- (6) At the very top of the second layer  $z_1^+$ , I can decompose  $P_1-V_{z1}$  data into up-going and down-going pressure waves,  $U_1^+(t)$  and  $D_1^+(t)$ , using  $c_1$  that has already been obtained in step (4);
- (7) Unlike  $D_0^+(t)$  which has a single seismic event, the down-going  $D_1^+(t)$  now may have a train of events because the interface at  $z_1$  can constantly reflect

waves downward. The upgoing  $U_1^+(t)$  should be composed of many seismic events too;

(8) As the down-going  $D_1^+(t)$  can be regarded as an input signal and the up-going  $U_1^+(t)$  as an output. I then deconvolve  $D_1^+(t)$  from  $U_1^+(t)$  and obtain a reflection response of the medium ( $z > z_1$  part and with a transparent boundary condition at  $z_1$ ) due to a down-going impulsive plane wave initiated at  $z_1^+$ . Here  $D_1^+(t) * R(t) = U_1^+(t)$  where  $*$  is the convolution operation. In the deconvolution, the response  $R(t)$  must be causal,  $R(t) = 0$  for  $t < 0$ . Now, I can loop this process recursively from step (4) to step (8) with a stopping criterion in the next step (9);

(9) Because the seismic data recording time length is finite and each depth extrapolation (Step (4)) will shift the up-going wave  $U(t)$  to the negative time direction. At sufficiently large depth  $z$ , the up-going wave will be all zero, and this is the stopping criterion for DWI.

It can be seen that DWI does not need an initial global model to start with. It integrates imaging and inversion as a single step, and it is recursive and always convergent.

## 2.3 Two synthetic examples

Here I present two synthetic examples to illustrate the application and effectiveness of the 1D DWI approach in a 1D stratified layered medium with plane wave incidence and constant density. In the first model, the free surface boundary conditions are set

on the top boundary, and half-spaces boundary conditions are set on the bottom boundary. In the second model, both the top and bottom boundaries are set up as half-spaces boundary conditions.

The first model is built of nine layers. Here I used one period of a 5Hz Sin function as the source wavelet. The source is at 0.45 km depth, and the receiver is at 0.55 km depth. Using the recorded  $P$  and  $V_z$  waveforms together with the first layer's velocity, I obtain the up-going and down-going pressure fields using equation (2.1) and apply the 1D DWI algorithm to invert the velocity model given as red line in Figure 2.2. From the records (Figure 2.3), I can see due to the relatively large value of layers' thicknesses, every event can be recognized easily, including first reflections, surface reflections, and multiples. Using the DWI algorithm, all this information could be fully utilized and yield a very precise inversion result comparing with the true model (Figure 2.2).

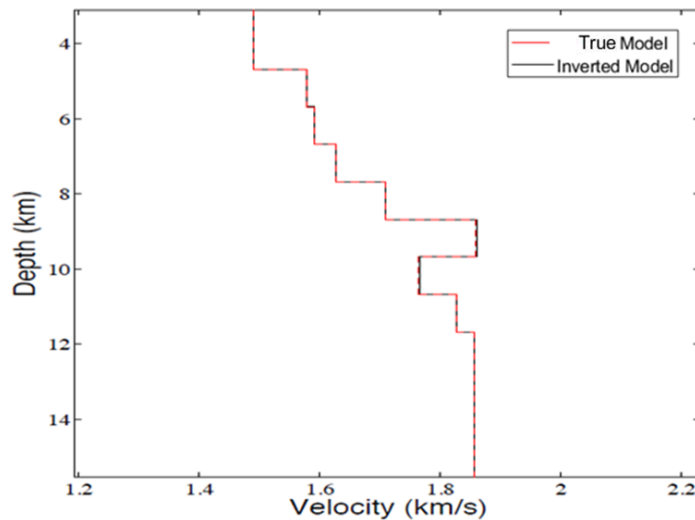


**Figure 2.2:** True model (red line) VS the DWI inverted model (black line).

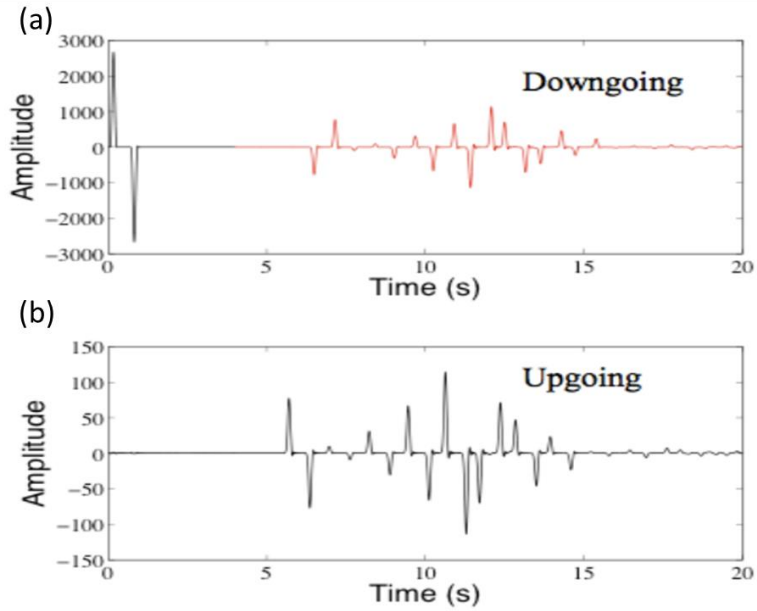


**Figure 2.3:** The down-going (a) and up-going (b) wavefields calculated from the record. Note the red part in the down-going time series is amplified by ten times.

The second test model is a layered medium given by the red line in Figure 2.4. Unlike the first model, this model is built by hundreds of thin layers, the thickness of these layers are all 3 meters. The plane wave source depth is 20 m. The source wavelet is a Gaussian wavelet acquired by integrating a 20 Hz central frequency Ricker wavelet twice in time. Therefore, the wavelength is about 100 m, which is large compared to the 3m layer thickness. The receiver is at 40 m depth, recording both  $P$  and  $V_z$  waveforms. The recorded waveforms are complex due to the internal multiples (Figure 2.5). However, the DWI can still successfully recover the model sound speed profile as the blue line in Figure 2.4. In fact, the DWI captures all physics, and the DWI inversion must use all wave types.

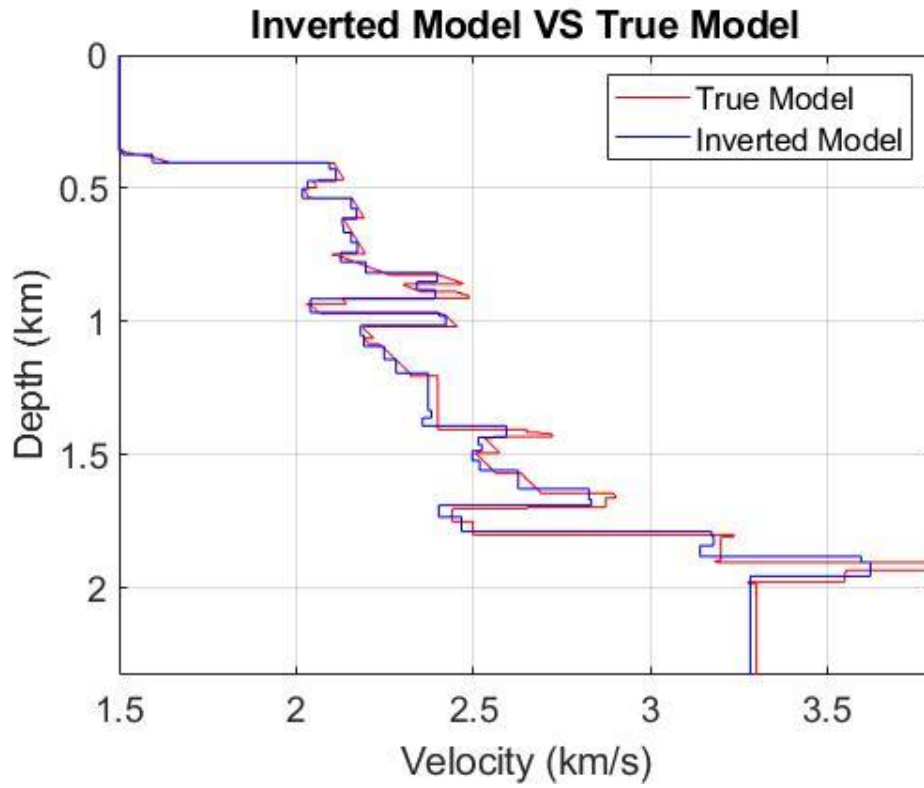


**Figure 2.4:** Comparison between the true model (red line) and the DWI inversion result (blue line).

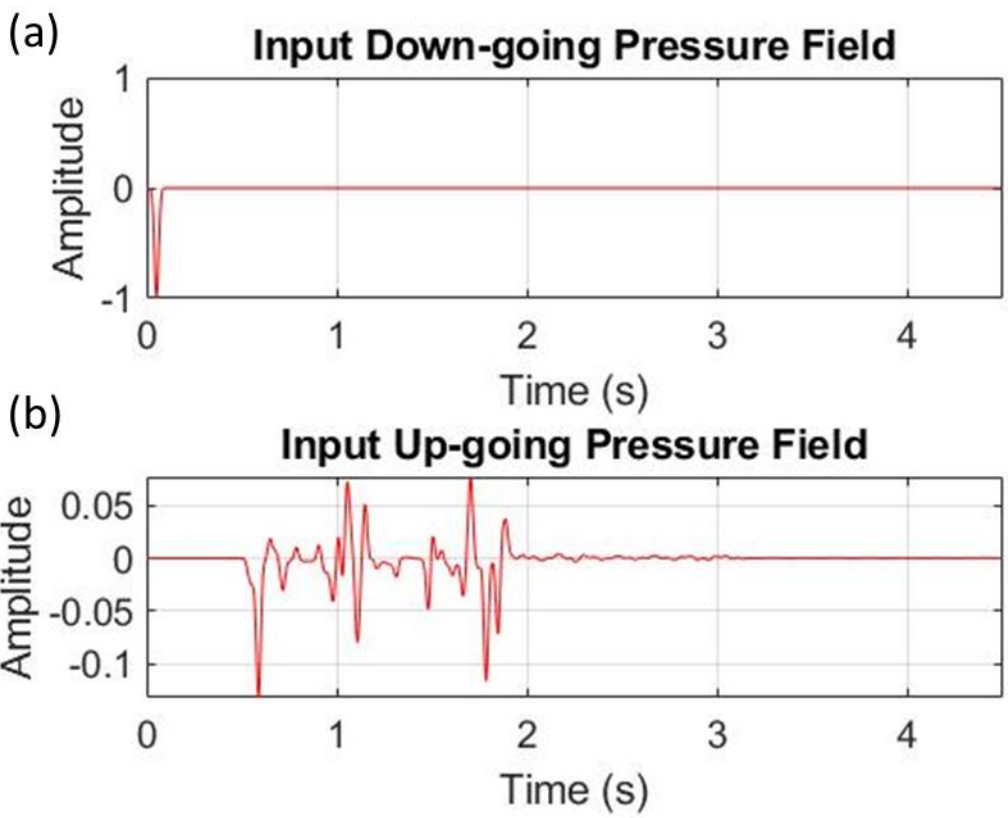


**Figure 2.5:** The down-going (a) and up-going (b) wavefields calculated from the record. Note the red part in the down-going time series is amplified by ten times.

## 2.4 Discussions

As discussed in the Introduction, the gradient-based full waveform inversion (FWI) is just one of many types of waveform inversion strategy. In the FWI, the interaction between the background wavefield and the unknown scatters is treated as a single-scattering Born scattering, which is valid if the scatter's size is small relative to the

wavelength (implies low frequency wave) and the velocity perturbation is weak. Consequently, the FWI needs to start from an accurate global low-wavenumber model or needs low-frequency data. This also means that the FWI is likely to succeed if the unmodeled scattered field (e.g., the difference between the observed data and the modeled data) is weak and can be modeled by the Born scattering.

In contrast, the DWI builds on the explicit use of the time-space causality. The causality allows us to perform waveform inversion locally. It reduces the global nonlinear optimization to many local inversions. Therefore, a global starting model for the DWI is not necessary. The DWI builds the model in a shallow-to-deep fashion until all recorded data is used due to its finite recording length. It is interesting to note that Kolb et al. (1986) found that “progressive downward determination of the velocity distribution“ was better in overcoming the “local minimum“ issue in the FWI. While the FWI is likely to succeed when the unmodeled field is weak, the DWI works well if the unmodeled scattered field is a strong signal.

## **2.5 Conclusions**

The DWI scheme I proposed here is a methodology to fit the entire waveform under the caveat that no initial global model and no model updating and iterations are needed. This method relies on the causality of the wavefield. It builds the model outward recursively from the source/receiver region. The DWI combines seismic imaging and inversion into a single step. The DWI fits the earliest part of the

waveform at each recursion step and represents a local fitting, therefore less computational time. Both primary and multiples are automatically taken into account in the DWI algorithm. The DWI offers the possibility to circumvent several significant challenges in the traditional FWI, including sensitive model dependence, local minima in the optimization, and slow or no convergence.

## **Chapter 3. DWI for density and velocity simultaneously in a 1D stratified layered acoustic medium with plane wave incidence**

In this chapter, I extend the DWI scheme by integrating the density inversion, using seismic recorded from a non-zero incident plane wave. A numerical example is presented to support the new framework.

### **3.1 Introduction**

Seismic full waveform inversion (FWI), formulated originally by (Lailly 1983, Tarantola 1984), is a powerful process in subsurface velocity model building. The goal of the FWI is to find a model such that the model-predicted waveforms fit the observed waveforms. Since the FWI is an iterative gradient-based method, its success depends on how far the initial model differs from the true model (Virieux and Operto 2009). The limitation of the iterative FWI scheme was recognized early on (Gauthier et al. 1986, Tarantola 1986, Mora 1987, Bourgeois et al. 1989). Tarantola (2005, p.128) pointed out that the local Fréchet gradient used in the FWI is equivalent to the single scattering Born approximation. Therefore the performance of the FWI relies on an accurate and long-wavelength initial velocity model, in which case the Born approximation is more accurate. In the Born single scattering, low-frequency seismic data are needed to invert for low-wavenumber/large-scale structures (Wu and Zheng 2014). However, due to the lack of low-frequencies ( $< 5$  Hz) in most reflection seismic data, most developments in the FWI have been focusing on how to recover

large-scale structural information without using low-frequency data. These developments include, for example, the Laplace FWI (Shin and Cha 2008, Shin and Ha 2008, Kim et al. 2013), envelope inversion (Wu et al. 2014, Luo and Wu 2015, Chen et al. 2018), intensity inversion (Liu et al. 2018, Liu et al. 2020), and the FWI using deep learning techniques (Richardson 2018).

To circumvent the challenges in the FWI, I proposed an alternative waveform inversion scheme (Liu and Zheng 2015, Liu and Zheng 2017), called the direct waveform inversion (DWI), to invert for subsurface models without an initial global model. The DWI combines seismic imaging and velocity model building into one single process. It is necessary for the input seismic data to include both free-surface and inter-bed multiples. Using surface recorded reflection seismic data, the DWI is able to deliver accurate P-wave velocity inversion results without using an initial global model for both 1D and 2D layered models (Zheng and Liu 2020). Without a global model, the DWI inverts the model from shallow to deep depths. In this regard, the DWI is similar to the layer-stripping methods (Claerbout 1976) and the approach by Goupillaud (1961). However, there are important differences in the methods, particularly the explicit use of the time-space causality in the DWI.

The purpose of this paper is to examine the DWI's potential to simultaneously invert for velocity and density profiles for a 1d layered medium. It is noted the DWI is not constrained to 1d layered cases. (Zheng and Liu 2020) demonstrated the DWI also worked for 2d models for velocity profile inversion. Since multi-parameter

attributes of rock strata are important for understanding subsurface properties and reservoir characterization, I have seen that multi-parameter the FWI methods had also been proposed to invert for not only P-wave velocity but also S-wave velocity, density, and seismic anisotropy (Sears et al. 2008, Brossier et al. 2009, Jeong et al. 2012, Warner et al. 2013, Alkhalifah and Plessix 2014). In the following sections, I extend the DWI formulation to the simultaneous inversion for layered velocity and density structures. A numerical example is given to demonstrate this methodology.

### **3.2 Inverting model's velocity and density using the DWI scheme**

In the previous 1D DWI scheme, I assume the density is constant throughout the model. For models of depth dependent density profiles, there were some relevant work by Coen in the 1980s (Coen 1981, 1981, 1981). In Coen's work, the density and velocity are inverted separately using a dataset from oblique incident plane waves based on the Gel'fand-Levitan-Marchenko (GLM) theory (Berryman and Greene 1980, Agranovich and Marchenko 2020). In my study, instead of applying the GLM theory, I directly use the incident angle ( $\theta$ )-dependence of the reflectivity,  $R(\theta)$ , to invert for both velocities and densities of a layered model. To achieve simultaneous inversion of velocities and densities, I show how to modify the steps in the previous section, respectively.

Assuming the wave is incident from medium-1 ( $\rho_1, c_1$ ) at an angle  $\theta$  to medium-2 ( $\rho_2, c_2$ ), I have the angle-dependent reflectivity

$$R(\theta) = \frac{\rho_2 c_2 \cos \theta - \rho_1 \sqrt{c_1^2 - c_2^2 \sin^2 \theta}}{\rho_2 c_2 \cos \theta + \rho_1 \sqrt{c_1^2 - c_2^2 \sin^2 \theta}}. \quad (3.1)$$

If I have two plane waves of two different incident angles  $\alpha$  and  $\beta$  and two amplitude ratios  $R_\alpha = R(\alpha)$  and  $R_\beta = R(\beta)$ , I can in principle determine  $c_2$ , and  $\rho_2$ , simultaneously.

To further improve the inversion's accuracy, I can make use of data from multiple incident angles ( $n \geq 2$ ) and minimize the objective function

$$J[\mathbf{R}(\theta_i), \mathbf{r}] = \sqrt{\sum_{i=1}^n |\mathbf{R}(\theta_i) - r_i|^2}. \quad (3.2)$$

In equation (3.2), for the plane wave at the incident angle  $\theta_i$ ,  $R(\theta_i)$  is the amplitude ratio calculated using the equation (3.1), and  $r_i$  is the measured amplitude ratio of the up-going and down-going pressure fields.

Assuming the incident angle is  $\theta$ , the steps of the DWI need to be adjusted as follows:

Firstly, I need to modify equation (2.2), the relationship between the pressure and vertical component of the particle velocity to

$$D - U = \rho c V_z / \cos \theta. \quad (3.3)$$

Secondly, the extrapolation of up-going and down-going pressure fields should be modified as

$$U_2^- = U_1^+ \exp(-i\omega\tau \cos \theta), \quad (3.4)$$

$$D_2^- = D_1^+ \exp(+i\omega\tau \cos \theta). \quad (3.5)$$

In addition, using the amplitude ratio  $R(\theta_i)$  from multiple incident angles,  $\theta_i$ , I can obtain  $c_2$  and  $\rho_2$  by either solving (3.1) directly or fitting equation (3.2). Compared with equation (3.1), equation (3.2) uses information from multiple traces and better handles errors from the data.

Finally, I need to use equations (2.1) and (3.3) to compose  $P$  and  $V_z$ .

### 3.3 Numerical Examples

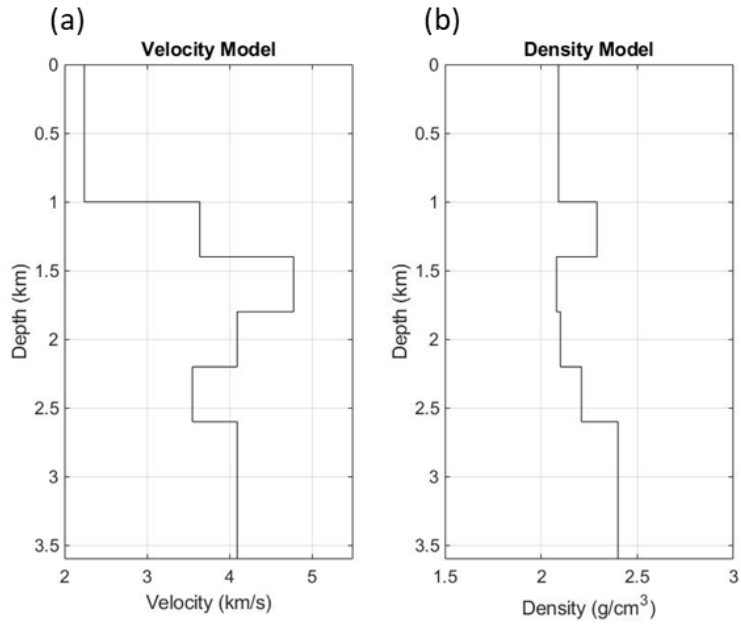
In this section, I present two synthetic examples to demonstrate the effectiveness of the proposed method: a simple layered model with six layers, and a complex layered

model with thirty-one layers. Both models are horizontally stratified. Within each layer, the velocity and density are constant. However, different layers have different properties. Both the top and bottom boundaries of the model are set up as half-spaces boundary conditions.

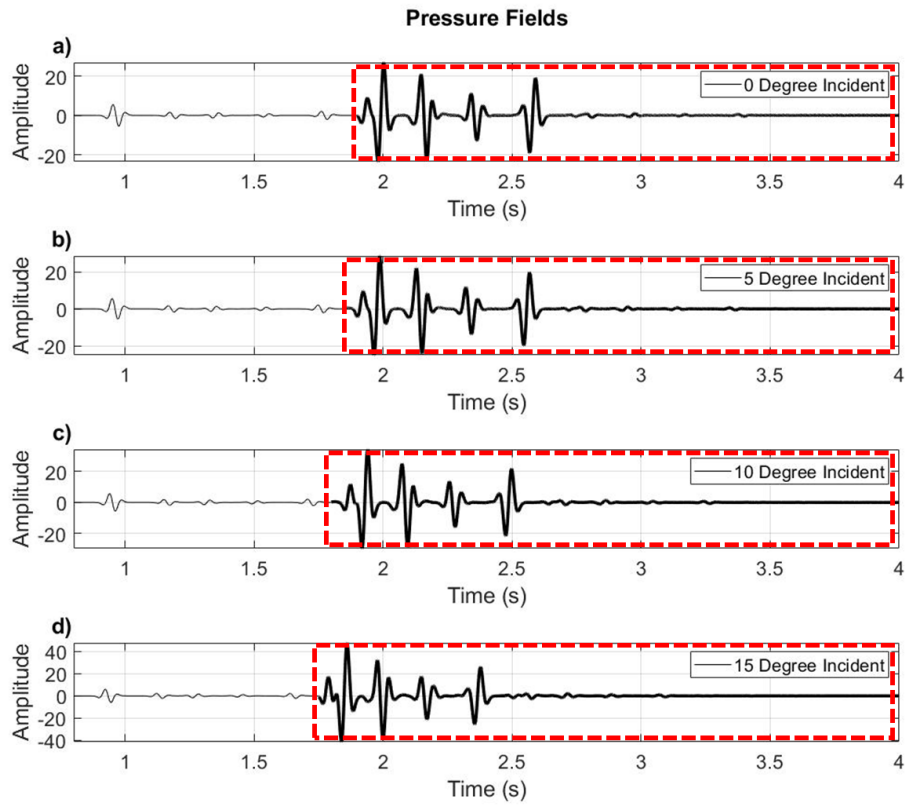
The synthetic data (pressure & particle velocity) in both examples are generated by a propagator matrix method (e.g., Eftekhar et al. 2018). The plane wave is injected at the depth of 0 m and propagated downward. The receivers are also placed at depth of 0 m. Both the pressure and particle velocity wavefields are recorded at a time sampling interval of 1ms.

### **Example 1.**

In the first example, different layers of the model (Figure 3.1) have the velocity contrasts up to 200%. Here I use a 15 Hz Ricker wavelet as the incident plane wave for the model (Figure 3.1). I conduct the modeling for four plane wave sources at different incident angles: 0, 5, 10, and 15 degrees. The waveform records of the pressure and the vertical component of particle velocity are shown in Figure 3.2.



**Figure 3.1:** Velocity (a) and density (b) profiles of the true model.



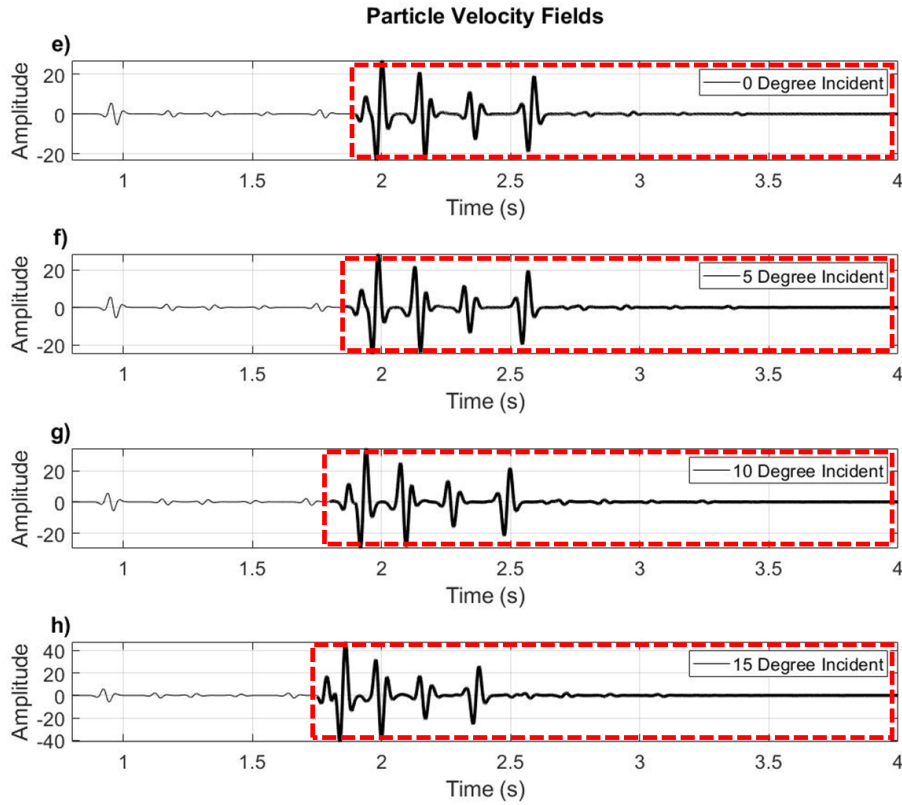


**Figure 3.2:** Recorded wavefields of pressure (a)-(d) and vertical component of particle velocity (e)-(h) in response to four different plane waves. The amplitudes in red dashed frames are amplified by 300 times.

In Figure 3.2, the recorded waveforms contain full waveform information of the pressure and vertical component of particle velocity fields, including the primary reflections and multiples.

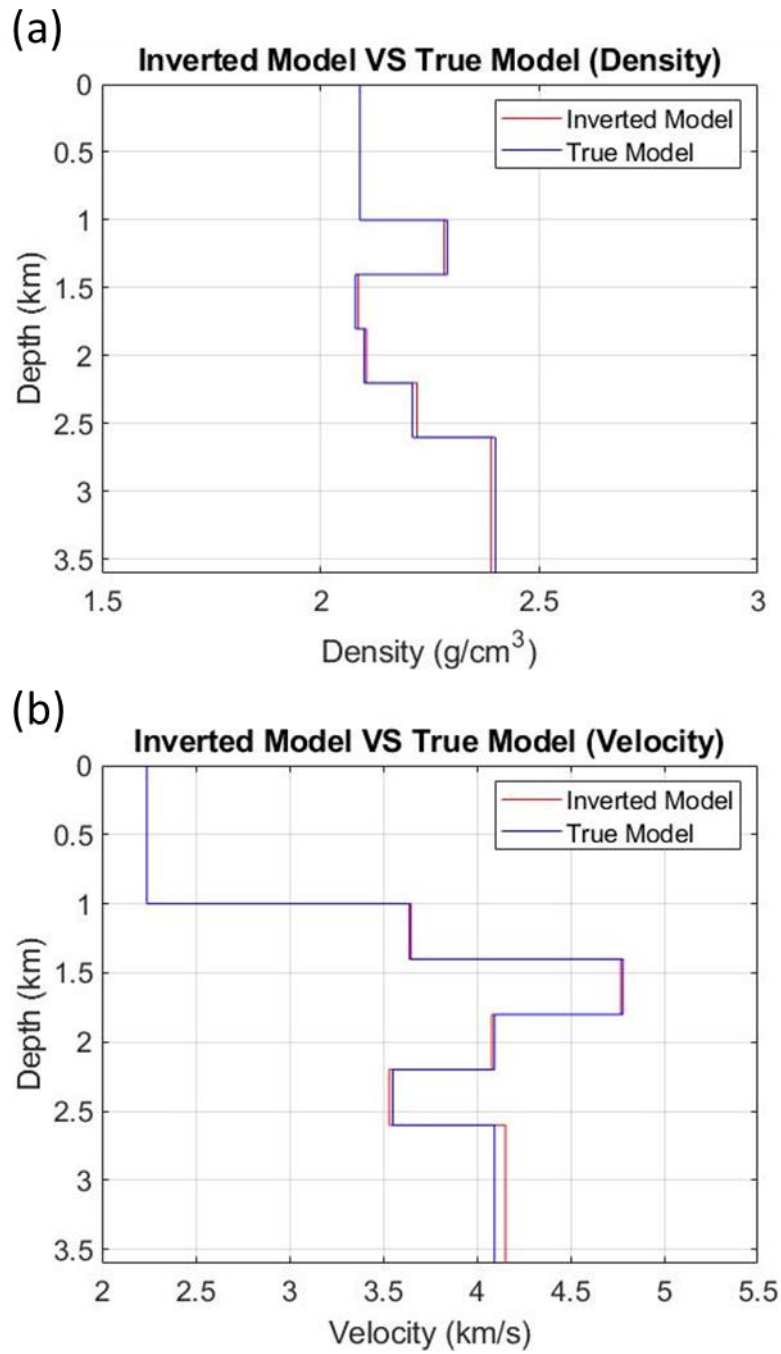


**Figure 3.3:** Comparisons between the DWI inversion result and true model on velocity (a) and density (b) models.

Using the input data shown in Figure 3.2 and following the DWI steps in the previous section, I invert for both the velocity and density of each of the model layers shown in Figure 3.3. I also lay out the misfit of velocities and densities between the inverted result and correct model in Table 3.1 (The misfits are calculated using the difference between the inverted and correct values divided by the correct values).

	Misfit of Velocity	Misfit of Density
Layer 2	0.28%	0.32%
Layer 3	0.26%	0.29%
Layer 4	0.34%	0.23%
Layer 5	0.54%	0.47%
Layer 6	1.33%	0.44%

**Table 3.1:** The misfit of velocities and densities between the inverted result and correct model (the velocity and density information of the first layer are known).

From Table 3.1, I can see most of the inverted results have a very high accuracy (less than 0.5%) except for the velocity of layer 6. This might cause by less waveform information in the up-going pressure field compared with the inversions in the layers above.

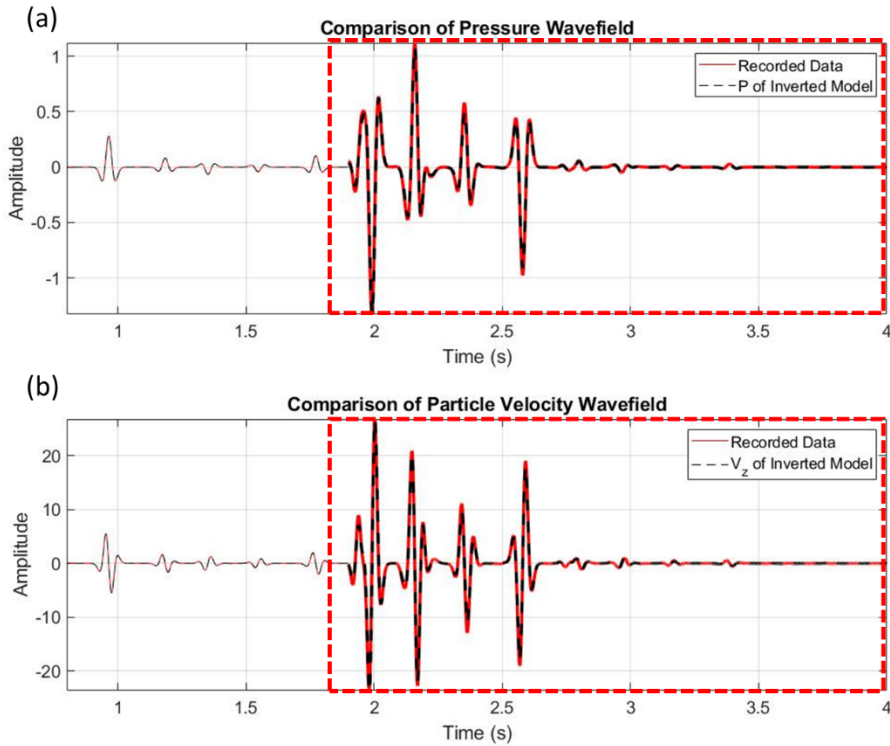
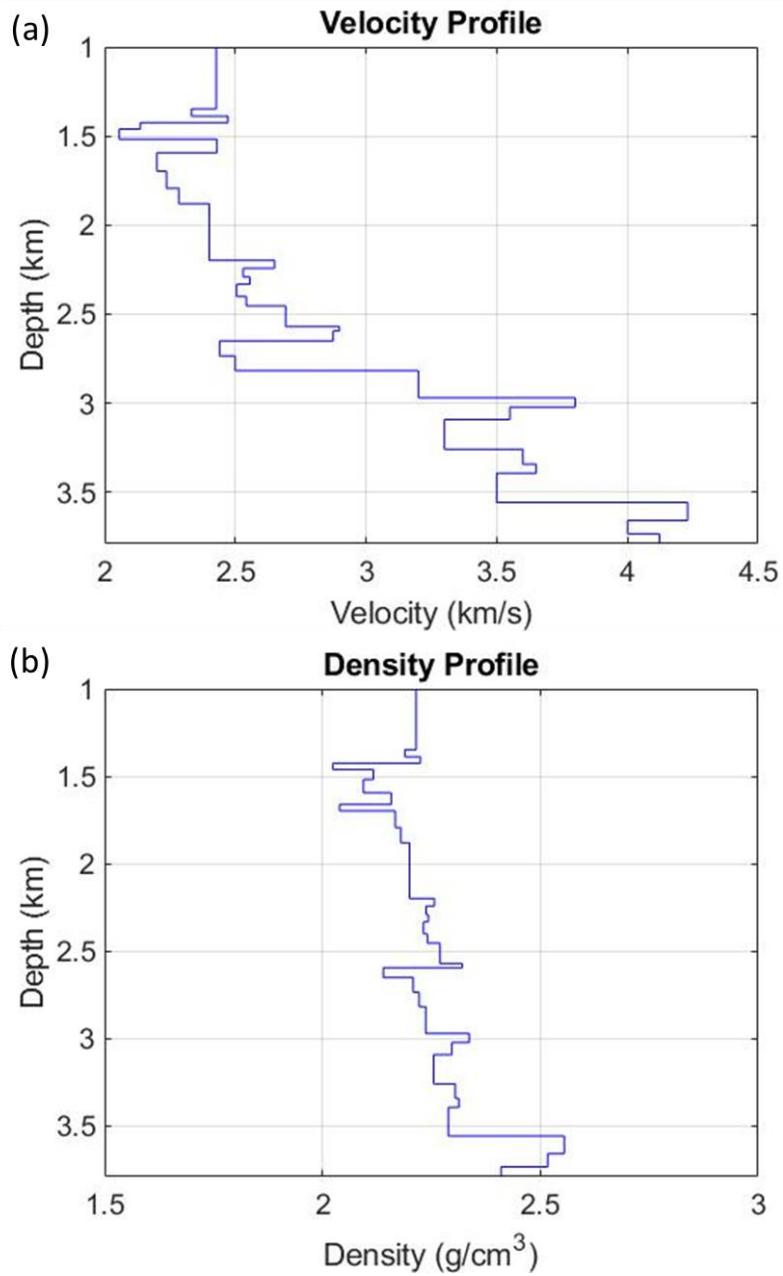


**Figure 3.4:** Comparisons of data (red) and synthetics (black) modeled using the DWI inverted model for pressure (a) and particle velocity (b) at the 0-degree incidence. Note the waveform amplitudes in the red dashed box are amplified by 300 times.

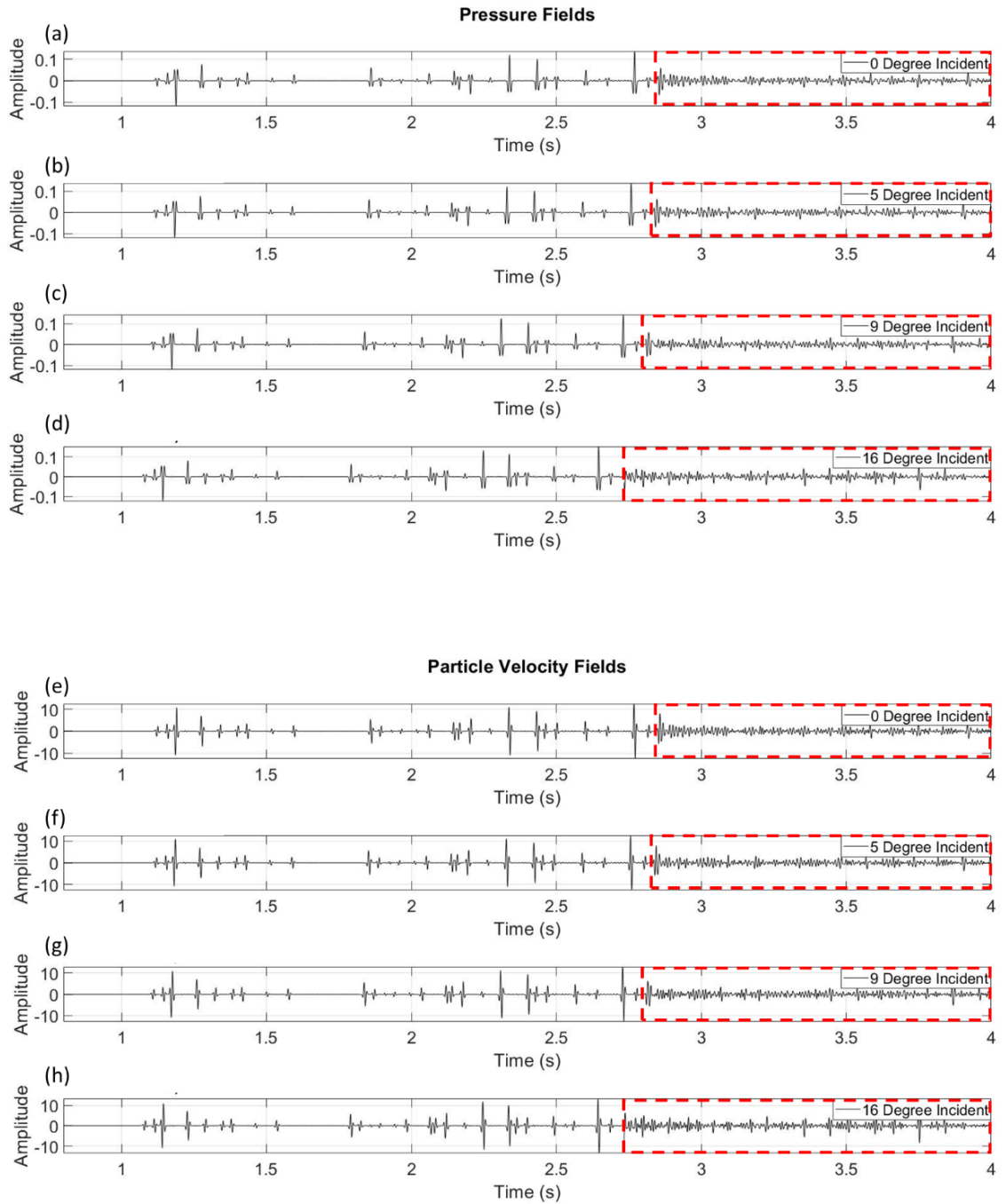
To check the validity of the inverted model in data space, I conduct a forward modeling process. The modeled waveforms using the DWI model fit the data very well (Figure 3.4). Both the primary reflections and the internal multiples get well recovered in the inverted model.

**Example 2.**

In the second example, I build a model with 31 velocity and density discontinuities (Figure 3.5). An 80 Hz Ricker wavelet is used as the incident plane wave, and the modeling is conducted for four plane wave sources at different incident angles: 0, 5, 9, and 16 degrees. The waveform recordings of the pressure and the vertical component of particle velocity are shown in Figure 3.6.

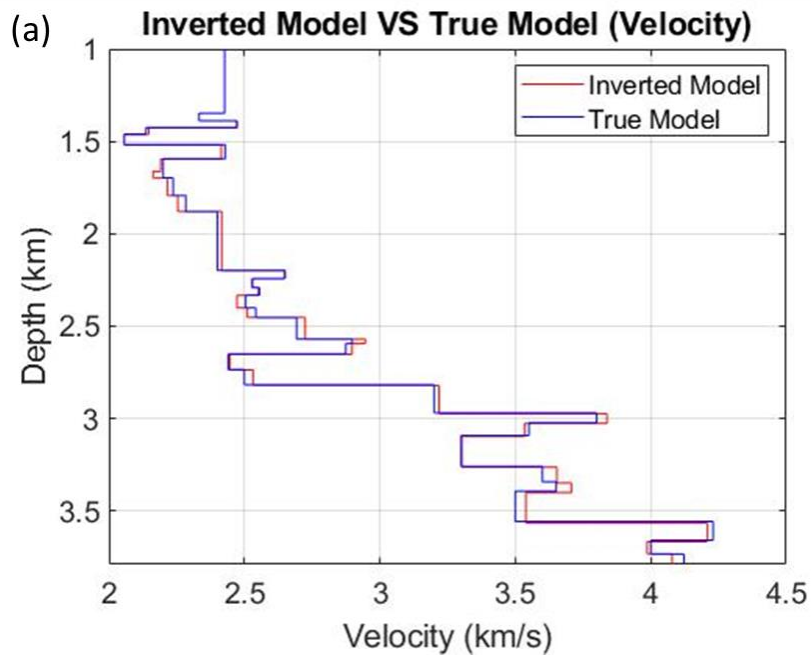


**Figure 3.5:** The velocity (a) and density (b) profiles of the true model for the DWI.



**Figure 3.6:** Recorded wavefields of pressure (a)-(d) and vertical component of particle velocity (e)-(h) in response to four different plane waves. The events in red dashed frames are amplified by 10 times.

Compared with the recorded waveforms in the first example (Figure 3.2), both the primary reflections and the internal multiples (Figure 3.6) are much more complicated. Using these data, I apply the DWI scheme and acquire the inversion results of velocity, density, and impedance models shown in Figure 3.7.



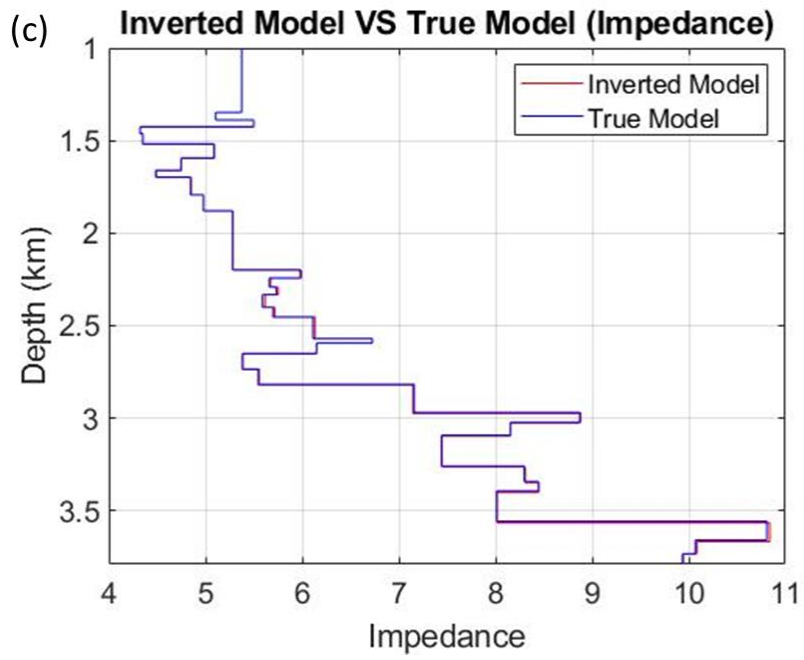
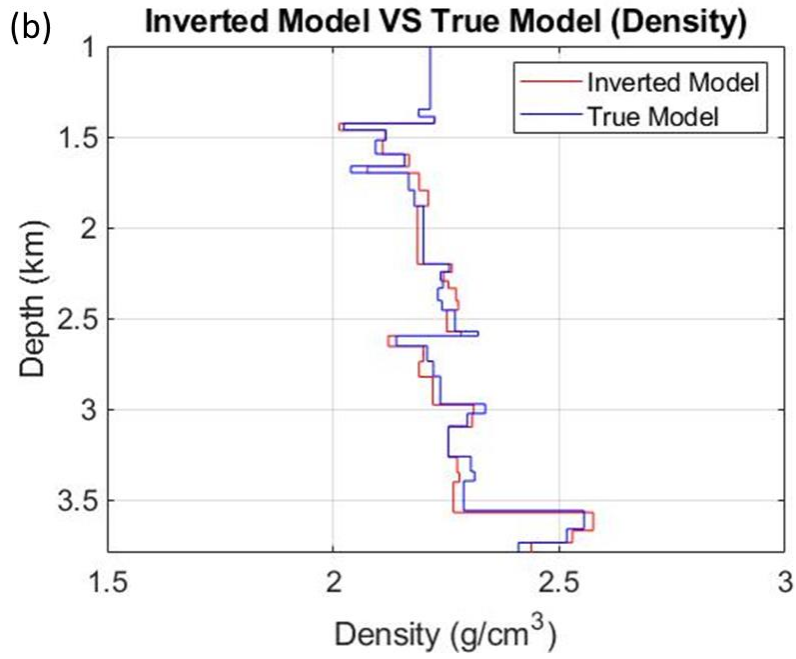


**Figure 3.7:** Comparisons between the DWI inverted model and true model on velocity (a), density (b) and impedance (c) models.

From Figure 3.7, I can see the DWI scheme almost fully recovers the true impedance model. Although there are some small misfits (less than 2%) for the velocity and density models, the inverted models still agree well with the true model. To further examine these misfits' influences, I also conduct a forward synthetic modeling same as example 1 based on the inversion result shown in Figure 3.8. The modeled waveforms using the DWI model fit the data very well, including the primary reflections and the internal multiples.

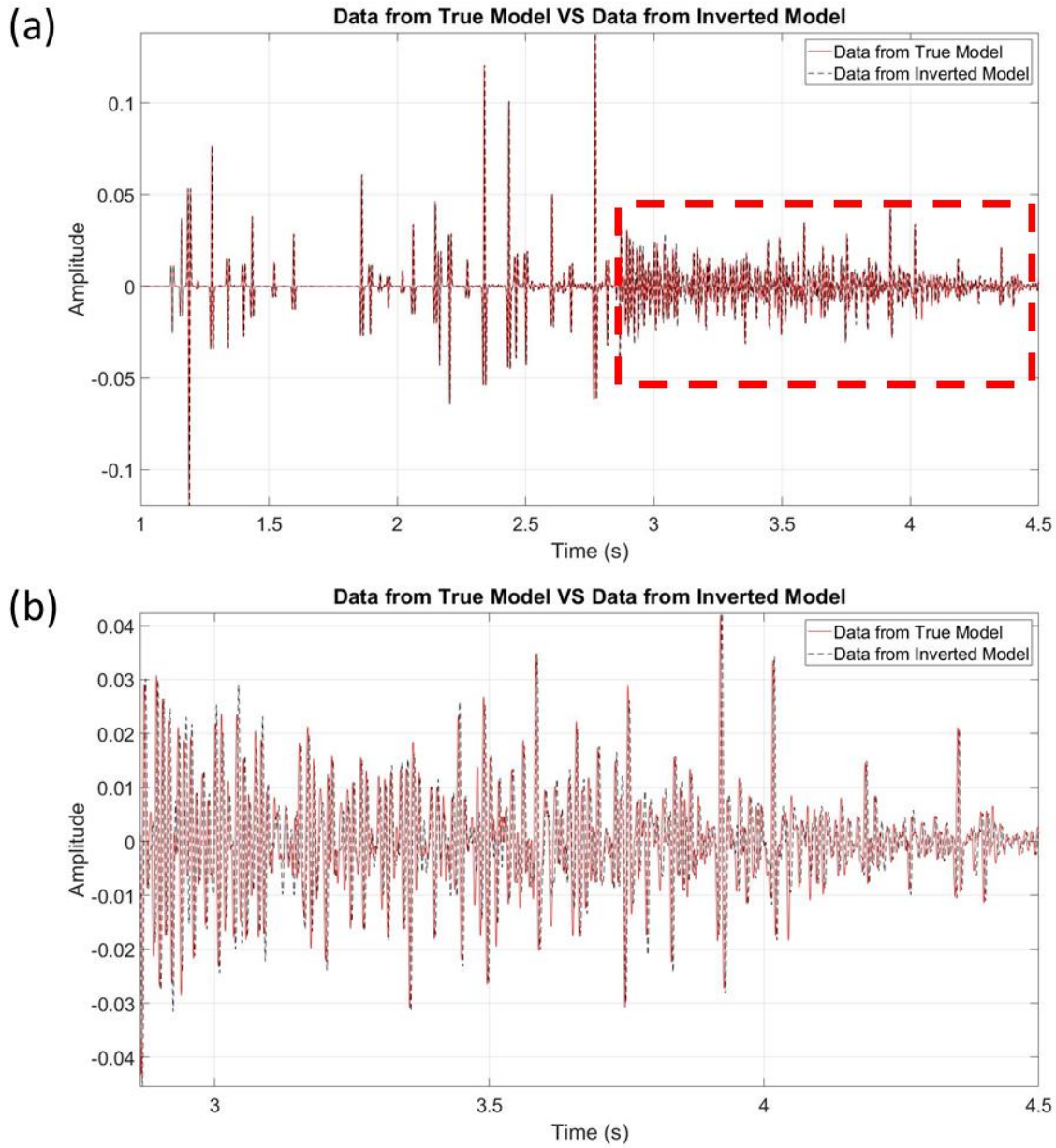


**Figure 3.8:** Comparisons of data (red) and synthetics (black) modeled using the DWI inverted model for pressure at the 0-degree incidence (a), the events in the red dashed box are amplified by 10 times. A zoomed in view of the events in the red dashed box are presented in (b).

### 3.4 Conclusion and discussions

Unlike the FWI, DWI does not rely on an initial global model to start the waveform inversion process. For the layered model with constant velocity in each layer, the DWI scheme converts the FWI global optimization problem into many localized reflectivity inversions using the causality principle. Hence it reduces the nonlinearity significantly. In the DWI, large-amplitude signals from strong-contrast anomalies are desired. In the FWI, if the misfit is large between the data and the initial model prediction, convergence can be a problem.

Another approach is the 1D density velocity inversion using the GLM theory (Wu and He 2020). This approach tries to invert the whole model in two-way traveltime then convert to depth. For the 1D problem, the time to depth conversion is easy to carry out, for 2D and 3D problems, a velocity model must be obtained as prior. However, for the DWI, the inversion is localized, and the inverted model is automatically in the depth domain.

I propose a new DWI scheme to simultaneously invert for the subsurface velocity and density properties, using multiple plane waves. Using recorded seismic data, this

method inverts for the model parameters locally from shallow to deep depths recursively. I used a numerical example to demonstrate the feasibility of this method.

## **Chapter 4. DWI for velocity in the 2D irregular bounded layered acoustic medium with point source**

In this chapter, based on the 1D DWI approach, I develop a direct waveform inversion (DWI) scheme to map subsurface velocity and reflectivity structures in 2D space. A numerical example is presented to support the new framework.

### **4.1 Introduction**

Seismic waveform inversion is among the most advanced approaches of seismic imaging to map subsurface structures and properties. Full-waveform inversion (FWI) studies (Lailly 1983, Tarantola 1984, Pratt et al. 1998, Pratt 1999, Pratt and Shipp 1999, Virieux and Operto 2009, Tao and Sen 2013) aim to find a subsurface model by solving a nonlinear optimization problem to match the recorded seismic waveforms using model prediction through an iterative perturbation approach.

The success of the FWI methods depends on the following: an accurate initial global velocity model, an optimization strategy to avoid local minima in inversion, and efficient propagators for rapid iteration and convergence (Pratt et al. 1998, Pratt 1999, Pratt and Shipp 1999, Virieux and Operto 2009). In addition, the successful application of the conventional FWI highly depends on the availability of the low-frequency data due to the single scattering approximation. However, a recent work by Wu and Zheng (2014) indicates the inadequacy of the single-scattering perturbation

assumption for modeling transmission waves through a strong velocity interface such as salt boundaries.

To deal with these requirements and challenges, several approaches have been developed in the FWI studies. For instance, the T-matrix method improves the convergence behavior and reduces the number of iterations by including higher-order non-linear terms in the inversion (Wu et al. 2014, Wang et al. 2017); the envelope inversion scheme alleviates the local minimum issue by introducing more low-frequency information into the inversion (Wu and Zheng 2014); and combining the traditional first-arrival traveltime tomography with the FWI has achieved satisfactory results (Liu and Zheng 2015, Liu and Zheng 2017).

Besides the perturbation-based approaches, methods based on inverse scattering series also play a significant role in studying and understanding the inversion problem. Weglein and his colleagues extended the early works of (Moses 1956, Razavy 1975) and developed the inverse scattering method (Weglein et al. 1997, Weglein et al. 2000, Weglein et al. 2001, Weglein et al. 2003). The inverse scattering method is a direct non-linear inversion with the advantage of not requiring prior knowledge of an initial velocity model. However, the convergence of the whole series is very weak (Prosser 1969, Prosser 1976, Prosser 1980, Prosser 1982, Weglein et al. 1997). To solve the convergence problem, Weglein and his colleagues also introduced the concept of “subseries”. The subseries are isolated from the whole series according to different tasks and converge. On the other hand, Yao et al. (2014) proposed another direct non-linear inversion scheme using the Volterra inverse

scattering series. Based on the previous work from Sams and Kouri (1969), the converging behavior of the Volterra series is guaranteed in the forward modeling. However, the inverse scattering series (ISS) using the Volterra series still suffers a convergence problem. Eftekhar et al. (2018) introduced the Shanks transform and achieved convergence acceleration.

Recently, Wapenaar et al. (2014) and Slob et al. (2014) presented the Marchenko imaging method based on the 1D focusing approach by Rose (2002). Using an estimated background velocity model and surface seismic record, the Marchenko imaging method can focus the wavefield to any point in the subsurface by fitting the Marchenko-type equation iteratively. This method virtually moves the seismic sources and receivers to a deeper depth, and the focused wavefield only contains the reflections coming from below. The Marchenko Imaging method provides a new solution for imaging for the mediums having complex overburden structures, but it needs an accurate velocity model. Earlier notable works on Marchenko (GLM) inversion include Ware and Aki (1969) and Berryman and Greene (1980). Berryman and Greene (1980) showed the equivalence between the Goupillaud method of inversion (Goupillaud 1961) and the Marchenko integral equation.

I first go through all the necessary steps, such as establishing suitable extrapolation and separation procedures to adopt the DWI idea from 1D to 2D problems. With numerical examples, I demonstrate the process in detail and study how the large velocity variation and lateral geometric variation impact the 2D DWI scheme.

## 4.2 Inverting model's velocity using the 2D DWI scheme

### 4.2.1 Separate & Extrapolate wavefields in a layered medium

In the 2D DWI, I consider a 2D model with irregular layers (Figure 4.1). Within each irregular layer, the medium is homogenous. The source is a point source in the first layer, which radiates spherical waves. The main differences between the 2d DWI and the 1d DWI are the propagating behavior of the wavefields and the geometries of the layer boundaries.

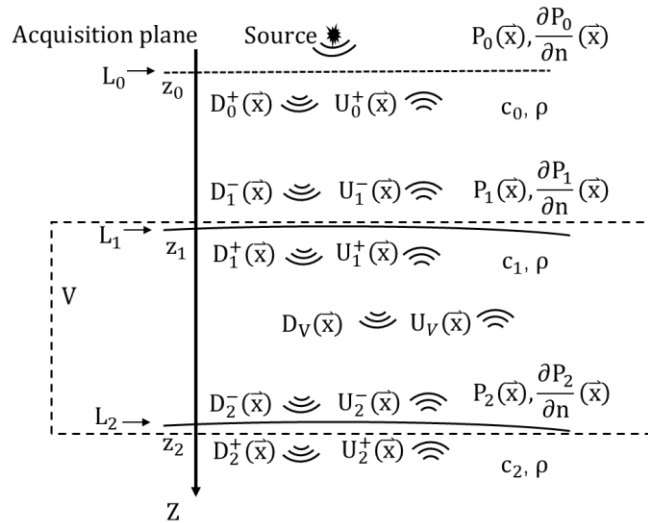


**Figure 4.1:** Wavefields in a 2D layered model.  $c_0, c_1, c_2$  are the velocities of each layer. The whole model has a uniform density value  $\rho$ .

In Figure 4.1,  $L_0$  is the acquisition plane below the source in the first layer,  $L_1$  and  $L_2$  are the upper and lower boundaries of the second layer. The whole volume of the second layer  $V$  is indicated by the dashed box. On  $L_0$ ,  $L_1$  and  $L_2$ ,  $P$  and  $\frac{\partial P}{\partial n}$  are the pressure and normal particle velocity fields,  $D$  and  $U$  with superscripts “-” and “+” are the up-going and down-going pressure fields, where “-” indicates the pressure fields on the upper side of the boundary, “+” indicates the pressure fields on the lower side of the boundary.  $D_V$  and  $U_V$  are the up-going and down-going pressure fields of any point below  $L_1$  in  $V$ .

#### 4.2.2 Decompose & extrapolate the wavefields in a 2D layered model

In a 2D layered model with point source incidence, the wavefields are spherical waves, and the layer interfaces could be curved. As a result, decomposition and extrapolation of the wavefields are not as easy as plane waves in the 1D case. In this section, I look for a new scheme to first decompose  $P_1$  and  $\frac{\partial P_1}{\partial n}$  into  $D_1^+$  and  $U_1^+$  on  $L_1$ , then extrapolate into  $D_V$  and  $U_V$ .

I start with the boundary integral equation in the frequency domain (e.g., Ge and Chen 2008) to calculate the wavefields in  $V$

$$P(\vec{x}) = \int_{L_1 \cup L_2} \left[ \frac{\partial P(\vec{x}')}{\partial n'} G(\vec{x}, \vec{x}') - P(\vec{x}') \frac{\partial G(\vec{x}, \vec{x}')}{\partial n'} \right] dS(\vec{x}'). \quad (4.1)$$

In equation

(4.1),  $\vec{x}$  is an arbitrary point in  $V$ ,  $n'$  is the normal direction of the surface element  $ds(\vec{x}')$ ,  $P(\vec{x}')$  and  $\frac{\partial P(\vec{x}')}{\partial n'}$  are the pressure and normal particle velocity fields (apart from the impedance constant) at  $x' \in L_1 \cup L_2$ , and  $G(\vec{x}, \vec{x}')$  is the causal Green's Function between point  $x$  and  $x'$ . In the mathematical language of the Huygens-Fresnel principle, equation

(4.1) represents the wavefields at any interior point of  $V$  is the sum of the boundary sources (monopoles and dipoles) on  $L_1 \cup L_2$  when no source exists in  $V$ .  $D_V$  and  $U_V$  could then be written as

$$D_V(\vec{x}) = \int_{L_1} \left[ \frac{\partial P_1(\vec{x}')}{\partial n'} G(\vec{x}, \vec{x}') - P_1(\vec{x}') \frac{\partial G(\vec{x}, \vec{x}')}{\partial n'} \right] dS(\vec{x}') \quad (4.2)$$

$$U_V(\vec{x}) = \int_{L_2} \left[ \frac{\partial P_2(\vec{x}')}{\partial n'} G(\vec{x}, \vec{x}') - P_2(\vec{x}') \frac{\partial G(\vec{x}, \vec{x}')}{\partial n'} \right] dS(\vec{x}') \quad (4.3)$$

As the DWI scheme starts from the top side of the model,  $P_2$  and  $\frac{\partial P_2}{\partial n}$  are not available at  $L_1$ , therefore I could not directly use equation (4.3) to calculate  $U_V$ . To address this issue, I use the anti-causal Green's Function  $G^*(\vec{x}, \vec{x}')$  to replace  $G(\vec{x}, \vec{x}')$  in equation(4.2). In this sense, instead of describing how the wavefield propagates forward in time,  $G^*(\vec{x}, \vec{x}')$  now describes how the wavefield propagates backward in time. Once I know  $U_1^+$  and  $\frac{\partial U_1^+}{\partial n}$  on  $L_1$ , I can further replace equation (4.2)'s  $P_1(\vec{x}')$  and

$\frac{\partial P_1(\vec{x}')}{\partial n'}$  by  $U_1^+(\vec{x}')$  and  $\frac{\partial U_1^+(\vec{x}')}{\partial n}$  to extrapolate the up-going pressure field backward as

below

$$U_v(\vec{x}) = \int_{L_1} \left[ \frac{\partial U_1^+(\vec{x}')}{\partial n'} G^*(\vec{x}, \vec{x}') - U_1^+(\vec{x}') \frac{\partial G^*(\vec{x}, \vec{x}')}{\partial n'} \right] dS(\vec{x}') \quad (4.4)$$

To calculate  $U_1^+$  and  $\frac{\partial U_1^+}{\partial n}$  on  $L_1$ , I consider equation

(4.1) when  $\vec{x}$  is on  $L_1$ ,

$$\begin{aligned} \frac{1}{2} P_1(\vec{x}) &= P.V. \int_{L_1} \left[ \frac{\partial P_1(\vec{x}')}{\partial n'} G(\vec{x}, \vec{x}') - P_1(\vec{x}') \frac{\partial G(\vec{x}, \vec{x}')}{\partial n'} \right] dS(\vec{x}') \\ &+ \int_{L_2} \left[ \frac{\partial P_2(\vec{x}')}{\partial n'} G(\vec{x}, \vec{x}') - P_2(\vec{x}') \frac{\partial G(\vec{x}, \vec{x}')}{\partial n'} \right] dS(\vec{x}') \end{aligned} \quad (4.5)$$

where P.V. stands for Cauchy's integral.

By substituting equation (4.3) into equation

(4.5),  $U_1^+$  could then be expressed as

$$U_1^+(\vec{x}) = \frac{1}{2} P_1(\vec{x}) - P.V. \int_{L_1} \left[ \frac{\partial P_1(\vec{x}')}{\partial n'} G(\vec{x}, \vec{x}') - P_1(\vec{x}') \frac{\partial G(\vec{x}, \vec{x}')}{\partial n'} \right] dS(\vec{x}')$$

$$U_1^+(\vec{x}) = \frac{1}{2} P_1(\vec{x}) - \text{P.V.} \int_{L_1} \left[ \frac{\partial P_1(\vec{x}')}{\partial n'} G(\vec{x}, \vec{x}') - P_1(\vec{x}') \frac{\partial G(\vec{x}, \vec{x}')}{\partial n'} \right] dS(\vec{x}'), \quad (4.6)$$

$\frac{\partial U_1^+}{\partial n}$  could also be calculated by applying an additional differential operator  $\frac{\partial}{\partial n}$  on

both sides of equation (4.6)

$$\frac{\partial U_1^+(\vec{x})}{\partial n} = \frac{1}{2} \frac{\partial P_1(\vec{x})}{\partial n} - \text{H} \int_{L_1} \left[ \frac{\partial P_1(\vec{x}')}{\partial n'} \frac{\partial G(\vec{x}, \vec{x}')}{\partial n} - P_1(\vec{x}') \frac{\partial^2 G(\vec{x}, \vec{x}')}{\partial n' \partial n} \right] dS(\vec{x}'), \quad (4.7)$$

where  $\text{H}$  represents a Hadamard finite part integration.

In summary, start from  $P_1$  and  $\frac{\partial P_1}{\partial n}$ , I firstly use equations (4.6) and (4.7) to calculate

$U_1^+$  and  $\frac{\partial U_1^+}{\partial n}$ , then use equations (4.2) and (4.4) to extrapolate  $D_V$  and  $U_V$  to any point

in  $V$  below  $L_1$ .

### 4.2.3 Detect the lower boundary & apply the localized inversion

In the 1D DWI scheme, the reflectors could be located based on the time difference between the first events in the up-going and down-going on the top of each layer because the raypaths are all along the vertical direction. However, in a 2D layered model with a point source, the raypaths could not be well defined anymore.

Therefore, a new scheme is required to locate the reflectors.

Here I apply the idea of the reverse time migration (RTM) method (Baysal et al. 1983) to find  $L_2$ . I use  $D_1^+$  and  $U_1^+$  on  $L_1$  as a line of virtual sources and their responses, and use a homogeneous half space below  $L_1$  with  $c_1$  as the velocity model. Since the only goal here is locating  $L_2$ , I do not need the velocity information from the layers below  $L_2$ . By the time-space causality rule, I can get  $L_2$ 's approximate location from the shallowest focused area in the migrated image. To further determine  $L_2$ 's exact location, I need to examine the first events of the extrapolated  $U_1$  and  $D_1$  at every point in the focused area. For the points on the reflector, their first events have the same traveltimes.

After I locate  $L_2$ , I can calculate  $c_2$  by minimizing the objective function

$$J_{R_i, r_i} = \sqrt{\sum_{i=1}^n R_i - r_i^2}, \quad (4.8)$$

for point  $\bar{x}_1$  on  $L_2$ ,  $R_i$  is the amplitude ratio calculated using the angle-dependent reflectivity relation in equation (4.8) shown below, and  $r_i$  is the amplitude ratio calculated from the first events of  $U_2^-$  and  $D_2^-$ .

$$R_i = \frac{c_2 \cos \theta_i - \sqrt{c_1^2 - c_2^2 \sin^2 \theta_i}}{c_2 \cos \theta_i + \sqrt{c_1^2 - c_2^2 \sin^2 \theta_i}}, \quad (4.9)$$

where I can calculate the incident angle  $\theta_i$  at  $\bar{x}_1$  by the ray tracing scheme (e.g. Zhou 2014) based on the model information I already acquired.

Finally, at  $L_2$  I can calculate  $P_2$  and  $\frac{\partial P_2}{\partial n}$  by adding up  $U_2^-$  and  $D_2^-$ ,  $\frac{\partial U_2^-}{\partial n}$  and  $\frac{\partial D_2^-}{\partial n}$  respectively using equation (4.10) and (4.11) shown below

$$P_2 = U_2^- + D_2^-, \quad (4.10)$$

$$\frac{\partial P_2}{\partial n} = \frac{\partial U_2^-}{\partial n} + \frac{\partial D_2^-}{\partial n}. \quad (4.11)$$

By now, I have built the recursive process of the DWI scheme in the 2D layered model. As the inversion goes deeper, when no focused reflectors could be found in the migrated image, I stop the DWI.

### 4.3 Numerical examples

In this section, I present a synthetic example to demonstrate the validity of this method. For the model, I consider a layered 2D model with irregular layer boundaries (Figure 4.2). The velocity is uniform within each layer, and the density is uniform throughout the whole model. Both the top and bottom boundaries of the model are half-spaces.

For the forward modeling process, I use a 2D acoustic finite difference method to compute the seismic data. The model has a 5 m grid size and 1 ms time step. I conduct 3 forward modeling processes with source  $S_1$ ,  $S_2$  and  $S_3$  placed at  $x_1=1.0$  km,  $z_1=0.1$  km;  $x_2=1.5$  km,  $z_2=0.1$  km and  $x_3=2.0$  km,  $z_3=0.1$  km. The source wavelet is a Ricker wavelet of 20 Hz central frequency. A linear array of 600

receivers recording the pressure  $P$  and particle velocity  $\frac{\partial P}{\partial n}$  are placed in the first layer below the source at the depth of 0.19 km, the receiver interval is 5 m.

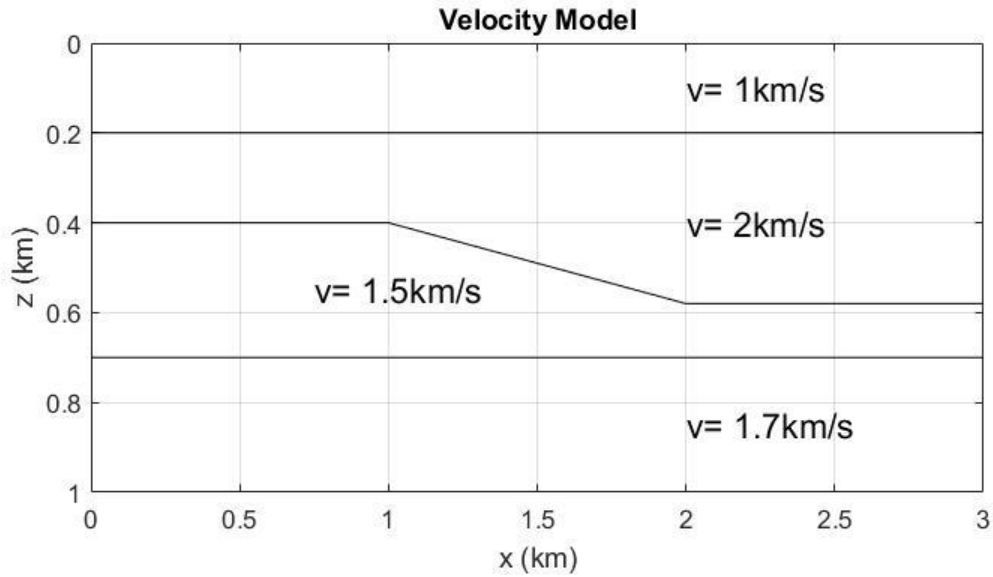


**Figure 4.2:** Velocity profile of the true model.

For the inversion process, here I use layer 2 as examples: start from layer 2's upper boundary, the pressure and particle velocity fields generated by the second source  $S_2$  at  $x = 1.5\text{km}$  are shown in Figure 4.3.

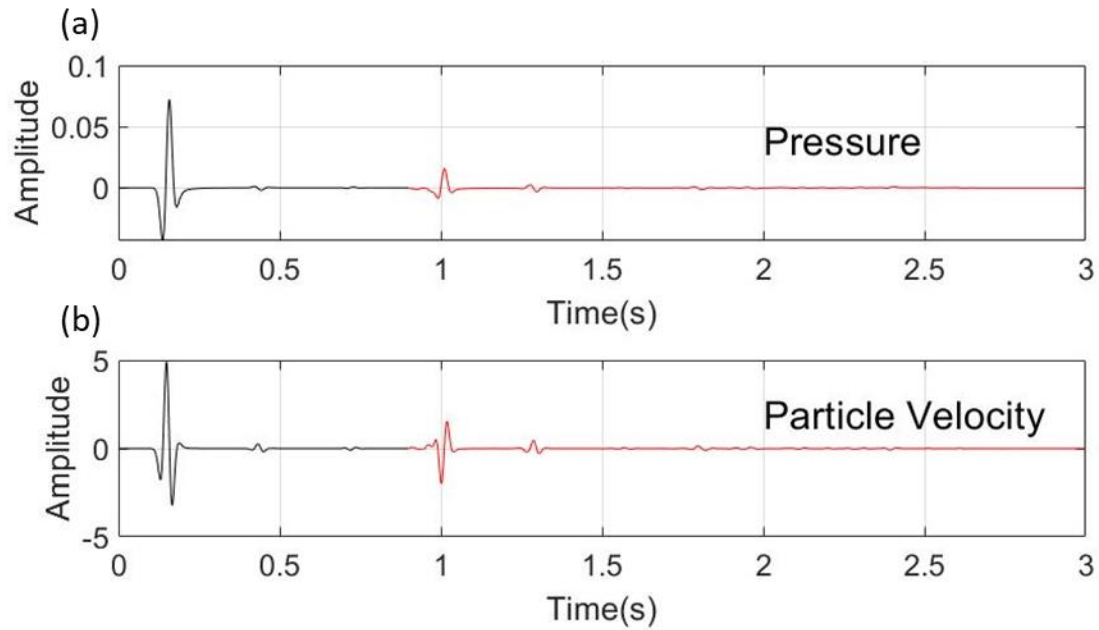


**Figure 4.3:** (a) The pressure field at layer 2's top. (b) The particle velocity field at layer 2's top. Events in red are amplified by 300 times.

Next, I decompose these wavefields by equations (2.1) and (4.6), the results are shown in Figure 4.4.

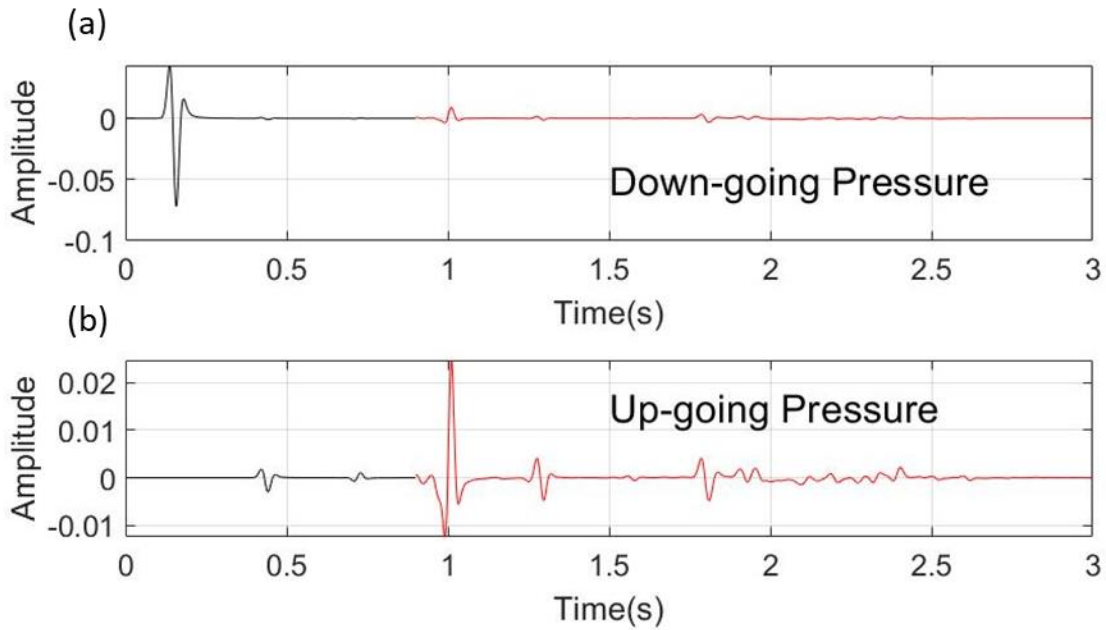


**Figure 4.4:** (a) The up-going pressure field at layer 2's top. (b) The down-going pressure field at layer 2's top. Events in red are amplified by 300 times.

I then propagate the decomposed wavefields downward into a homogeneous space with layer 2's velocity and apply the cross-correlation between two wavefields.

The migrated image is shown in Figure 4.5.

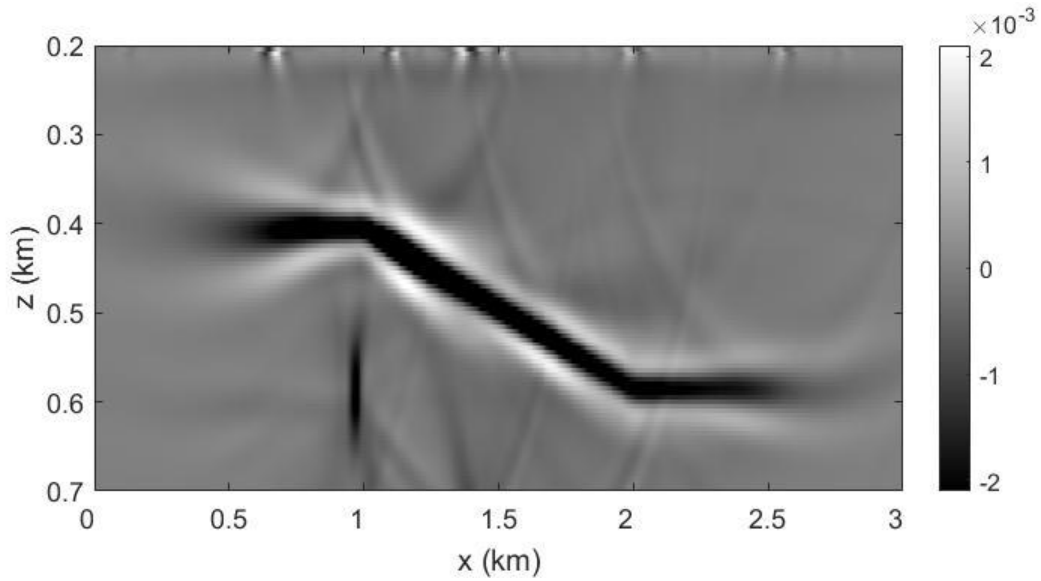


**Figure 4.5:** Migrated image by using a half space with constant layer 2's velocity as model and decomposed up-going and down-going pressure fields as input.

By analyzing the up-going and down-going pressure fields in the focused area in Figure 4.5, I can further determine the exact location of layer 2's lower boundary. The detailed comparisons at different depths but the same horizontal coordinate  $x = 1.5\text{km}$  are shown in Figure 4.6 and Figure 4.7.

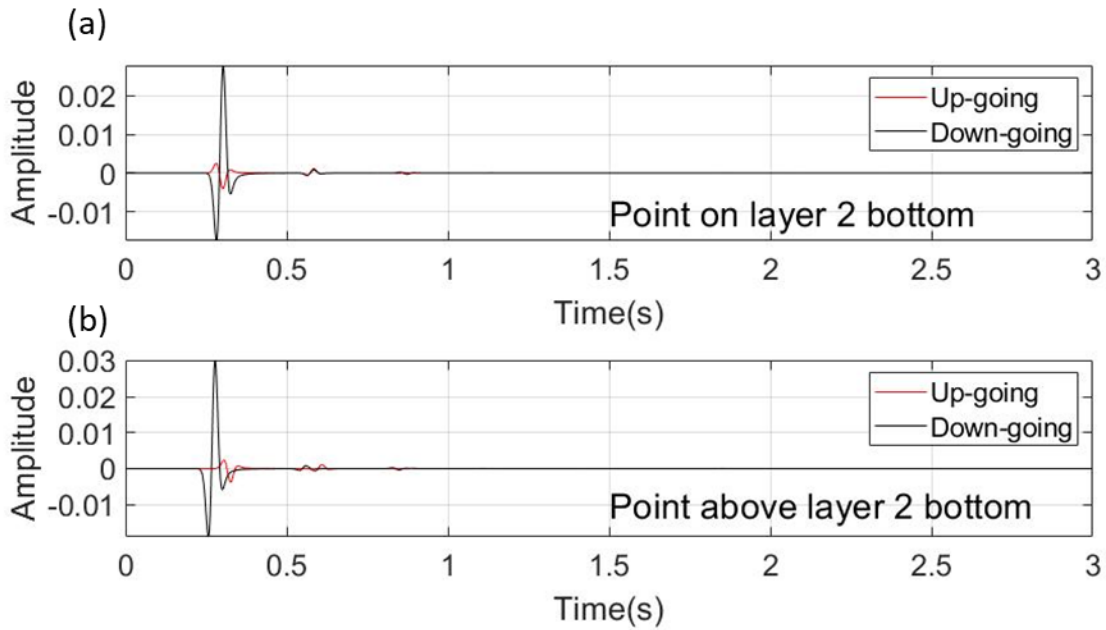


**Figure 4.6:** (a) The up-going and down-going pressure fields at point right on layer 2's lower boundary. (b) The up-going and down-going pressure fields at point one grid above layer 2's lower boundary.

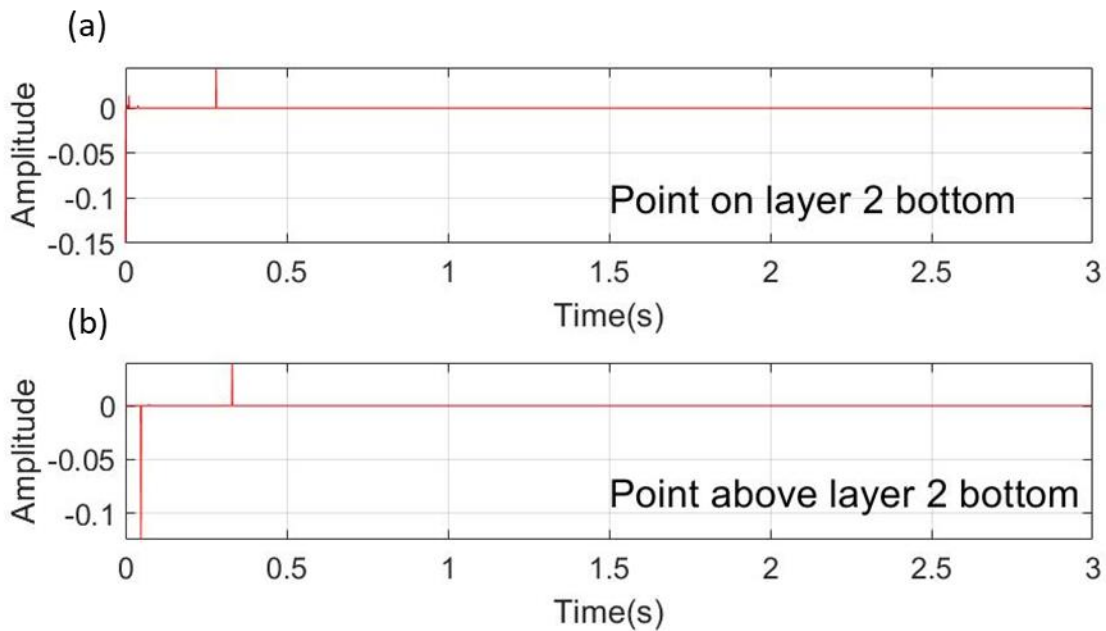


**Figure 4.7:** (a) Deconvolution results from the up-going and down-going pressure fields at point right on layer 2's lower boundary. (b) Deconvolution results from the up-going and down-going pressure fields at pointone grid above layer 2's bottom boundary.

At layer 2's lower boundary, the first events of the up-going and down-going pressure fields meet at the same time, and the first impulse of the deconvolved time series is at time 0. I then apply the inversion using equations (4.8) and (4.9) to calculate layer 3's velocity and apply equations (4.10) and (4.11) to calculate the full pressure and normal particle velocity fields. The calculated wavefields are shown in Figure 4.8

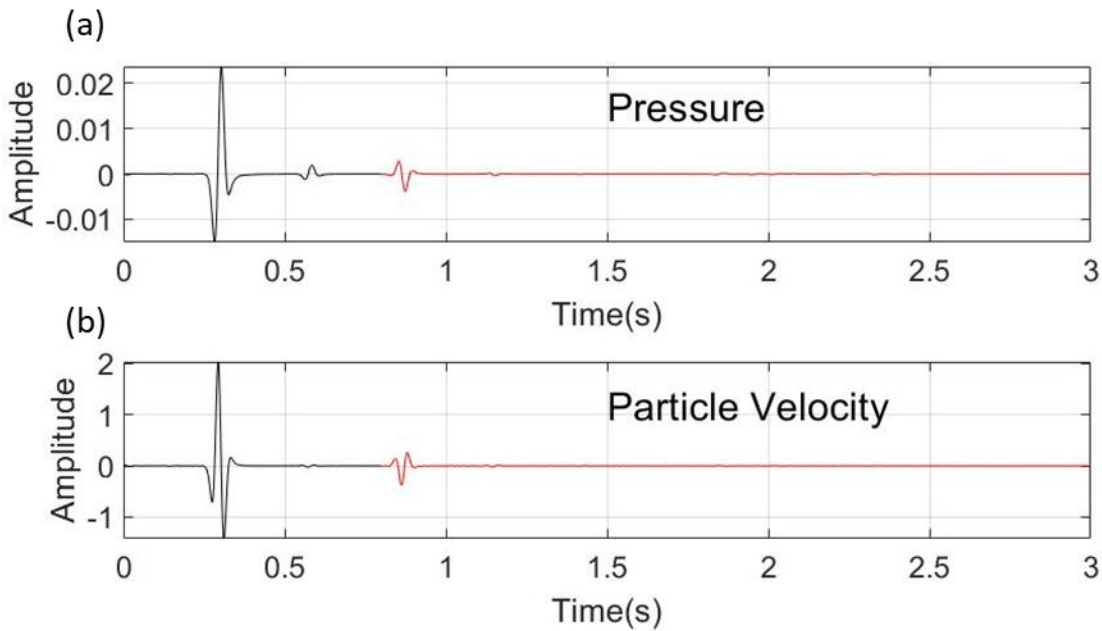


**Figure 4.8:** (a): The pressure wavefield at layer 2's bottom. (b): The particle velocity wavefield at layer 2's bottom. Events in red were amplified by 15 times.

Above are all the steps of the 2D DWI scheme's recursive process within one layer. By taking this process recursively, it is capable of mapping out the geometries and velocity properties of every layer without any prior knowledge of the model except the velocity of the first layer (with the assumption of the uniform density model).

In the following part, I present the final inversion result from the true model in Figure 4.2. The comparison between the true model and the inverted model is given in Figure 4.9. The comparison between the input dataset and the modeled dataset using the inverted model is shown in Figure 4.10.

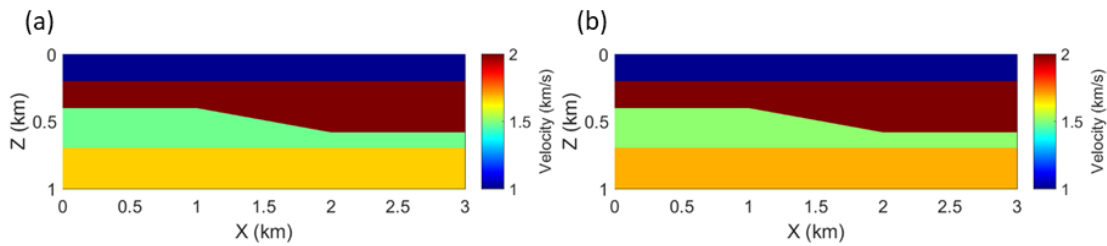


**Figure 4.9:** (a) The original velocity model (b) The inverted velocity model.

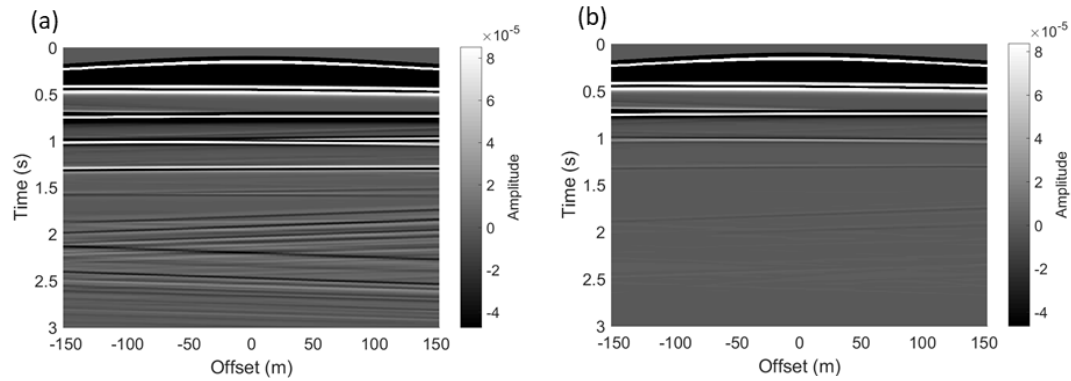


**Figure 4.10:** Gather of input pressure wavefield (a) versus gather of modeled pressure wavefield(b) from inversion result.

Figure 4.9 displays a very good reconstruction result on the velocity model above the irregular boundary, but a small misfit below, which is also revealed in Figure 4.10. The misfit in the deeper layers weakened the amplitudes of multiples. Nevertheless, the amplitudes and traveltimes of the primary reflections and multiples are still well matched, indicating the misfit is reasonable.

## 4.4 Discussions

One new feature of the 2D DWI algorithm is that I changed from a global scale approach to a local scale approach. Instead of inverting for all model parameters simultaneously, I start from the acquisitions and build the model parameters recursively, from the source and receiver layers to expand the solution downwards until reconstructing all model layers.

Compare with the 1D DWI scheme, the 2D DWI scheme has almost the same procedure for each recursive process but much more complicated details for the realization, which follows the fundamental principle of the DWI to focus on the space-time causal property of the wavefields and to use only the responsible parts of the waveform records in the imaging and inversion process.

In the 2D DWI algorithm, the decomposition and extrapolation processes are based on the boundary integral approach, which requires the integration interval to be either a closed space or of infinite length. Hence, I assume that all the model boundaries are long enough to ensure precision. However, the anti-causal Green's Function is not convergence as distance approaching infinity. In this situation, I can expect some artifacts in the calculated up-going pressure and particle velocity fields; this might bring in errors in the inverted results.

In the numerical example, I only tested 2D models with tilted layer boundaries and large velocity contrast, and it yielded satisfactory results. Clearly, further tests on more general types of model geometry are necessary to better investigate the feasibility, noise tolerance, and accuracy of the 2D DWI algorithm.

## **4.5 Conclusions**

I have extended the direct waveform inversion (DWI) scheme to 2D space from the previous 1D method. The methodology and numerical simulations show that the 2D

DWI is able to provide a promising alternative approach to the conventional FWI formalism. I have demonstrated with numerical examples that the DWI algorithm does not require an initial global model, and it maps the subsurface in a recursive fashion from shallow to deep depths. The DWI is unconditionally convergent since it uses recursion rather than iteration. I will be able to extend the DWI to map more complex structures in the future.

## **Chapter 5. DWI for velocity inversion in a 1D stratified layered acoustic medium with point sources**

In this chapter, I further modify the original 1D DWI scheme and present a new scheme able to reconstruct a 2D stratified layered model's velocity profile using the pressure and particle velocity fields from a point source. A numerical example is presented to support the new framework.

### **5.1 Introduction**

In the previous chapters, I proposed the DWI inversion scheme along with applications in both 1D and 2D stratified layered models. By strictly enforcing the time-space causality rule, the DWI scheme turns the non-linear global inversion problem into localized inversions at each layer. The wavefields are decomposed, extrapolated, and used for localized inversion in a recursive process from shallow to deep depth. Using the full waveform data, including primary reflections, free-surface, and inter-bed multiples, the DWI scheme doesn't rely on an initial global model and is able to provide an accurate reconstruction of the model's properties.

In this chapter, I present a modified 1D DWI scheme applicable with zero-offset seismic records generated by a point source in a 2D stratified layered model.

Unlike the previous 1D DWI scheme, the modified scheme does not rely on an accurate amplitude information. I first present the details of the new DWI scheme, then prove its feasibility using the inversion result from a numerical example.

## **5.2 Applying the modified 1D DWI scheme in 1D stratified layers with point source**

In a 2D stratified layered model with a point source (Figure 5.1), the wavefields are spherical waves and have different propagating behavior from plane waves. As a result, applying the original 1D DWI scheme (equation (2.1) and (2.2)) in Chapter 2 on the zero-offset record from the stratified layered medium creates errors. However, by comparing the results of applying the original 1D DWI scheme between the spherical wavefields and plane wavefields from the same model, some waveforms in the result of the spherical wavefields have the same traveltimes but different amplitudes compared with the events in the results of the plane wavefields. In this chapter, I use these waveforms as the events for my inversion, and the rest waveforms are treated as errors.

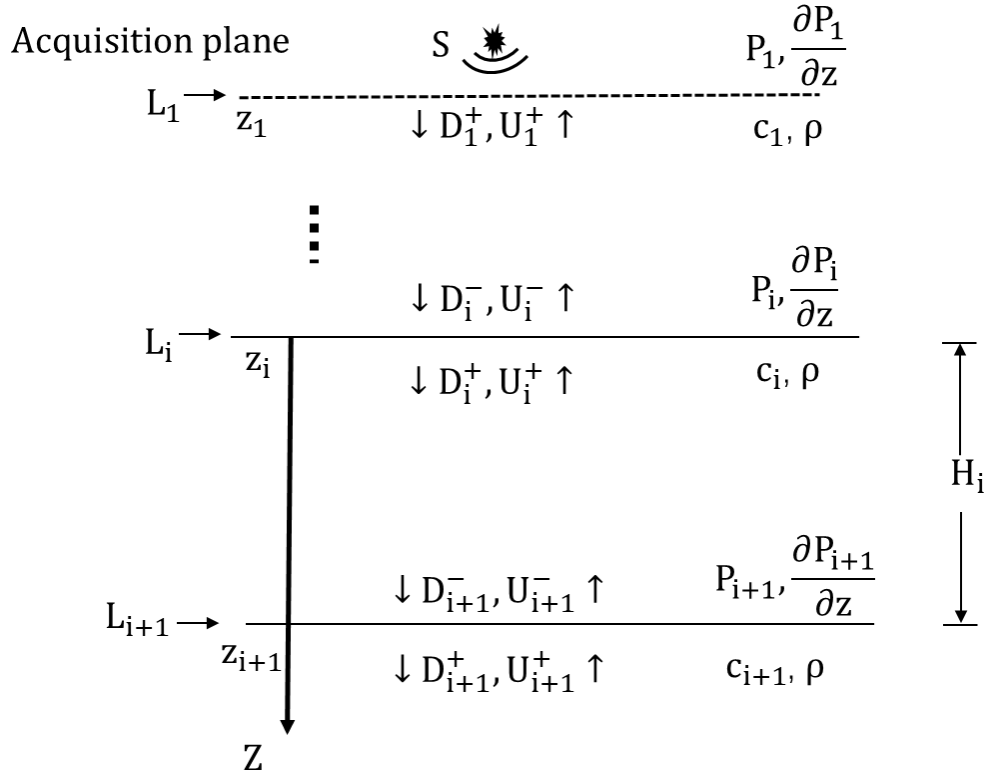


**Figure 5.1:** Wavefields in a 2D stratified layered model. The whole model has a uniform density value  $\rho$ .

In Figure 5.1,  $c_1$ ,  $c_i$ ,  $c_{i+1}$  are the velocities of the first,  $i^{th}$  and  $(i + 1)^{th}$  layer,  $H_i$  is the thickness of the  $i^{th}$  layer.  $S$  is the source wavelet.  $L_1$  is the acquisition plane below the source in the first layer,  $L_i$  and  $L_{i+1}$  are the upper and lower boundary of the  $i^{th}$  layer. On  $L_1$ ,  $L_i$  and  $L_{i+1}$ ,  $P$  and  $\frac{\partial P}{\partial n}$  are the pressure and normal particle velocity fields,  $D$  and  $U$  with superscripts “-” and “+” are the up-going and down-going pressure fields, where “-” indicates the pressure fields on the upper side of the boundary, “+” indicates the pressure fields on the lower side of the boundary.

In the DWI schemes, the localized inversion in the  $i^{th}$  layer has two goals: inverting for  $H_i$  and inverting for  $c_{i+1}$ . In this study, for the first goal, since the events in  $D_i^+$  and  $U_i^+$  have correct traveltimes, and the one-way traveltime can be retrieved from the first events in  $D_i^+$  and  $U_i^+$  once the errors are removed. For the second goal, since the amplitudes are erroneous in  $D_{i+1}^-$  and  $U_{i+1}^-$ , even if the errors are removed, a new method still needs to be established to calculate  $c_{i+1}$ .

To better illustrate the relation between the errors and events in  $D_i^+$  and  $U_i^+$  in the following sections, I represent them as below

$$D_i^+(t) = D_{\text{error}}(t) + D_{\text{event}}(t), \quad (5.1)$$

$$U_i^+(t) = U_{\text{error}}(t) + U_{\text{event}}(t). \quad (5.2)$$

where  $t$  is the time,  $D_{\text{error}}$  and  $U_{\text{error}}$  are the errors,  $D_{\text{event}}$  and  $U_{\text{event}}$  are the events having correct traveltimes but wrong amplitudes.

### 5.2.1 Applying 1D scheme on 2D data to invert for the current layer's thickness

In Chapter Chapter 2,  $H_i$  could be retrieved from the half of the time difference between the first events in  $D_i^+$  and  $U_i^+$ ,  $\tau$ . In this study, there are additional errors that need to be removed in  $D_i^+$  and  $U_i^+$  to locate the first events. To begin with, here I note the arrival times of the first events in  $D_i^+$  and  $U_i^+$  as  $\tau_{D_i}$  and  $\tau_{U_i}$ .

Since the first event of  $D_i^-$  and  $D_i^+$  have the same traveltime,  $\tau_{D_i}$  can be calculated from equation (5.3) using  $\tau_{D_{i-1}}$  and  $\tau_{U_{i-1}}$

$$\tau_{D_i} = \frac{\tau_{D_{i-1}} + \tau_{U_{i-1}}}{2}. \quad (5.3)$$

To find  $\tau_{U_i}$ ,  $U_{\text{error}}(t < \tau_{U_i})$  needs to be eliminated. As equation (2.1) and (2.2) describe a linear relationship between  $P_i$ ,  $\frac{\partial P_i}{\partial n}$  and  $D_i^+$ ,  $U_i^+$ ,  $U_{\text{error}}$  are actually part of  $P_i$  don't get correctly calculated. According to the time-space causality rule,  $P_i(t < \tau_{U_i})$  are the first arrivals and the internal multiples from layers above. Hence a forward modeling result  $P_i'$  based on the inverted information of layer 1 ... i-1 can be used to predict  $P_i$  for the part  $(t < \tau_{U_i})$  and  $U_{\text{error}}(t < \tau_{U_i})$ . In addition,  $P_i'$  can also be used to eliminate the part of  $U_{\text{error}}(t > \tau_{U_i})$  corresponding to the internal multiples from layers above coming after  $\tau_{U_i}$ . For the rest of  $U_{\text{error}}(t > \tau_U)$  corresponding to the events from deeper layers, although they can not be eliminated by the forward modeling process, these errors do not bother finding  $\tau_{U_i}$ .

Same as  $U_{\text{error}}$ , the part of  $D_{\text{error}}$  corresponding to the part of  $P_i$  from layers above can be predicted and eliminated by  $P_i'$ . The rest part of  $D_{\text{error}}$  corresponding to the events from deeper layers don't affect the inversion process.

## 5.2.2 Applying 1D scheme on 2D data to invert for next layer's velocity

In Chapter 2,  $c_{i+1}$  is calculated using the relation of the amplitude ratio of the first up- and down-going events,  $R_{i+1}$  and  $c_i, c_{i+1}$  in step (5). Considering the amplitude errors in  $U_{\text{event}}$  and  $D_{\text{event}}$ , I introduce a new factor  $f_{\text{error}}$ . Using  $f_{\text{error}}$  the relation of  $R_{i+1}$  and  $c_i, c_{i+1}$  becomes equation (5.4)

$$R_{i+1} * f_{\text{error}} = \frac{c_{i+1} - c_i}{c_{i+1} + c_i}, \quad (5.4)$$

where  $f_{\text{error}}$  is the factor to compensate for the amplitude error.

Without knowing  $f_{\text{error}}$ , equation (5.4) could not be used to invert for  $c_{i+1}$ . In this section, I present a strategy to invert for  $c_{i+1}$  without calculating  $f_{\text{error}}$ .

I start with a model of  $i+1$  layers. The first  $i$  layers of this model are based on the inverted information of layer 1 ...  $i-1$ . For the  $(i + 1)^{\text{th}}$  layer, I know the layer thickness  $H_i$  from the previous step in section 5.2.1. The model's bottom boundary is set as a free surface. I then perform another forward modeling process based on the new model and get the new dataset  $P_1''$  and  $\frac{\partial P_1''}{\partial n}$ . By applying the same modified 1D DWI scheme on  $P_1''$  and  $\frac{\partial P_1''}{\partial n}$ , the new model's up-going and down-going pressure fields  $U_{i+1}^-''$  and  $D_{i+1}^-''$  could be calculated at the bottom of the  $i^{\text{th}}$  layer. Since all the medium of the layer 1... $i$  are the same between this model and the original model,  $U_{i+1}^-''$  and  $D_{i+1}^-''$  have the same amplitudes errors as  $U_{i+1}^-$  and  $D_{i+1}^-$ . In this case, the

relation between the amplitude ratio of the first events in  $U_{i+1}^-$  and  $D_{i+1}^-$ ,  $R_{i+1}$ , can be written as below

$$R_{i+1} * f_{\text{error}} = -1. \quad (5.5)$$

Combining equation (5.4) and (5.5),  $f_{\text{error}}$  is canceled and  $c_{i+1}$  could be represented using  $R_{i+1}$ ,  $R_{i+1}$  and  $c_i$

$$c_{i+1} = c_i - 2c_i \frac{R_{i+1}}{R_{i+1} + R_{i+1}}. \quad (5.6)$$

In summary, for each recursive process of the modified 1D DWI scheme, here are the steps it consists of.

Step 1. Start from  $L_i$ , I decompose  $P_i$  and  $\frac{\partial P_i}{\partial n}$  into  $U_i^+$  and  $D_i^+$  using equations (2.1) and (2.2). I then calculate  $P_i^i$  based on all the inverted model above  $L_i$ . Using  $P_i^i$  I eliminate the part of  $U_{\text{error}}$  and  $D_{\text{error}}$  corresponding to the responses from layer 1 to  $i-1$ . Then I get  $H_i$  by multiplying  $c_i$  with  $\tau$ , which is half of the time difference between the first impulse in the up-going wave  $U_i^+$  and the first impulse in  $D_i^+$ .

Step 2. I extrapolate  $U_i^+$  and  $D_i^+$  to the bottom of the  $i^{\text{th}}$  layer (depth  $z_{i+1}$ ) in the frequency  $\omega$ -domain

$$U_{i+1}^- = U_i^- \exp(-i\omega\tau), \quad (5.7)$$

$$D_{i+1}^- = D_i^- \exp(+i\omega\tau). \quad (5.8)$$

Step 3. After calculating the amplitude ratio of the first events between  $U_{i+1}^-$

and  $D_{i+1}^-$ ,  $R_{i+1}$ , I perform another forward modeling process based on all the inverted model above  $L_{i+1}$  and set  $L_{i+1}$  as a free surface to get  $U_{i+1}^-$  and  $D_{i+1}^-$  and  $R_{i+1}$ . Using equation (5.6),  $c_{i+1}$  could be determined.

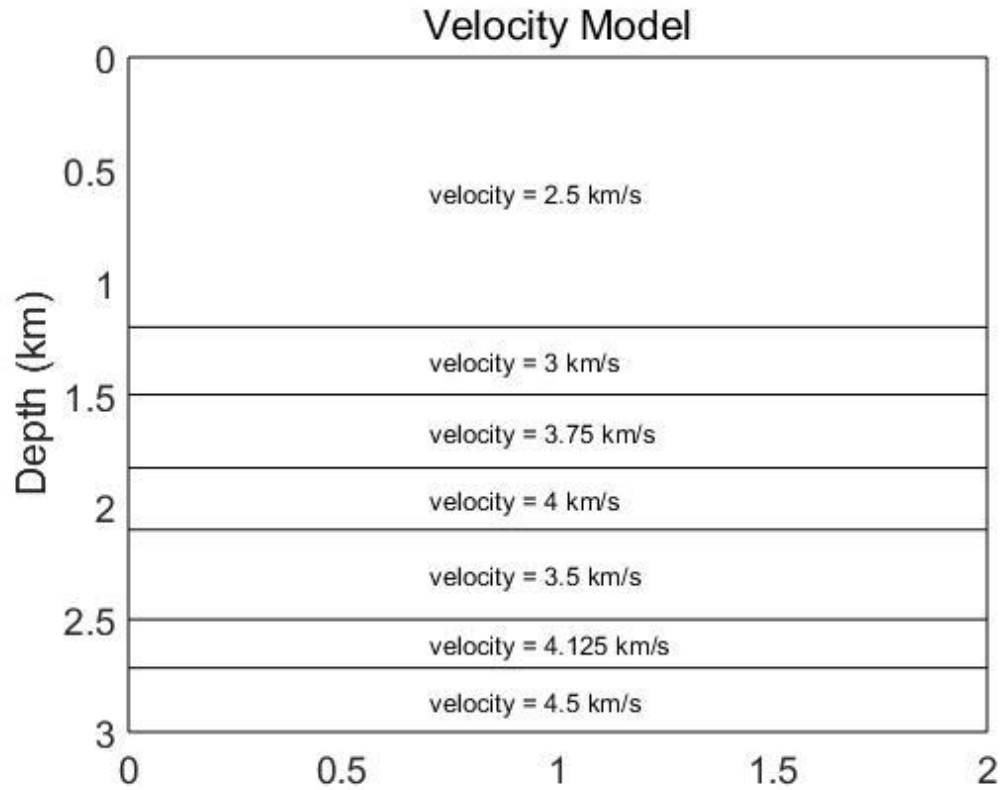
Step 4. Finally, with  $c_{i+1}$ ,  $D_{i+1}^-$  and  $U_{i+1}^-$ , I apply equation (2.1) and (2.2) again to get  $P_{i+1}$ ,  $\frac{\partial P_{i+1}}{\partial n}$ .

Start with the recorded dataset  $P_0$ ,  $\frac{\partial P_0}{\partial n}$ , and  $c_0$ , the above process inverts the parameters of each layer ( $c_i$ ,  $H_i$ ) from shallow to deep recursively. Note that, unlike the original 1D DWI scheme, the errors in this scheme make the waveforms in  $U_i^+$  are not becoming fewer and fewer as the inversion going deep. Therefore a target depth needs to be set to force the inversion to stop.

### 5.3 Numerical example

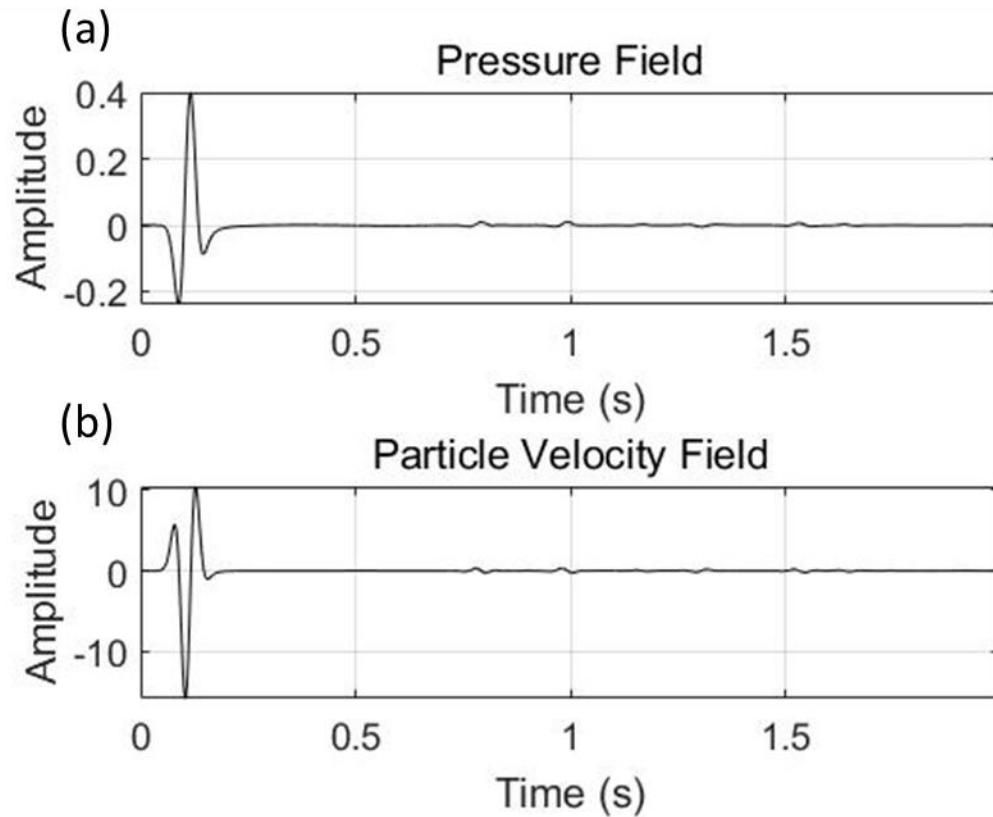
In this section, I present a numerical example to validate the method. The model I used here is a stratified layered 2D model (Figure 5.2). Both the velocity and density are uniform in each layer. Both the top and the bottom of the model are half spaces.

The synthetic wavefields are computed by a 2D finite difference method. The source is a 15 Hz Ricker wavelet point source placed at the depth of 0.25km, the pressure  $P$  and particle velocity  $\frac{\partial P}{\partial n}$  are recorded at 0.1km below the source. The model has a 5 m grid size, and the data are recorded at a 1 ms time step.



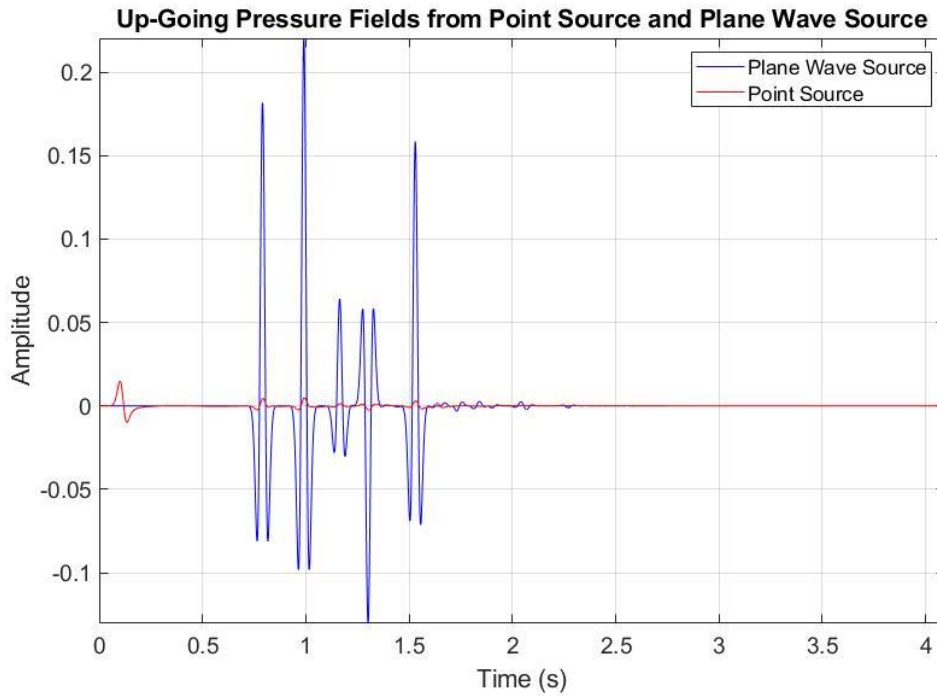
**Figure 5.2:** Velocity profile used for generating synthetic data

Figure 5.3 shows the recorded wavefields, including the pressure and vertical component of the particle velocity fields. These wavefields include both primary reflections and multiples.



**Figure 5.3:** Pressure(a) and particle velocity(b) fields record used for the inversion.

To illustrate the idea of errors and events in this study, I first present the comparison of the up-going pressure fields calculated at the receiver depth using the velocity profile in Figure 5.2 with a point source and plane wave incidence (Figure 5.4).



**Figure 5.4:** Comparison of the up-going pressure fields calculated at the receiver depth using the velocity profile in Figure 5.2 with a point source (blue) and plane wave incidence (red).

Compare the two results in Figure 5.4, although their amplitudes are different, some waveforms in the point source result still have the same traveltimes as the events in the plane wave incidence result. Based on the previous discussion, these waveforms are the events with correct traveltimes but wrong amplitudes. For the other waveforms in the point source result, they are considered as errors.

To better illustrate the process of removing the errors in step 1, here I use the deconvolved results from the up-going and down-going pressure fields at the top of layer 3 as an example (Figure 5.5).

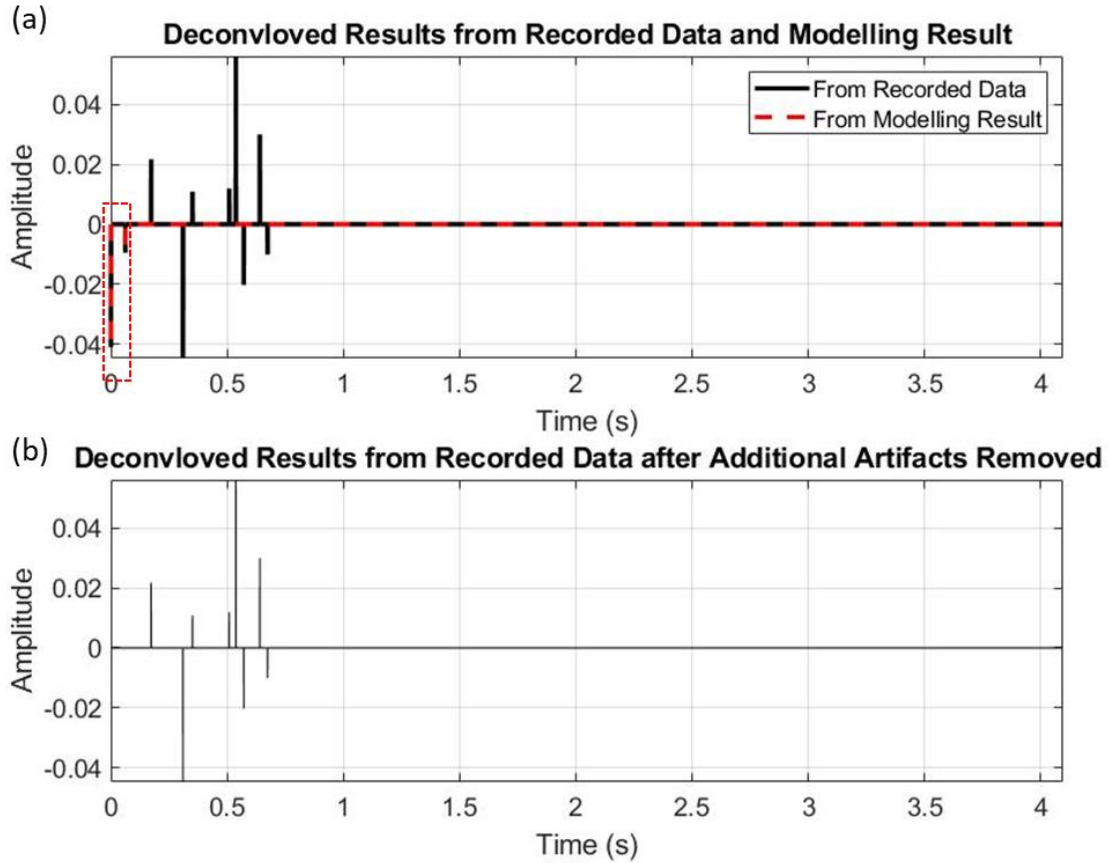


**Figure 5.5:** Result before(a) and after(b) removal of the errors at the third layer's top.

In Figure 5.5 (a), the black line is the deconvolved result from the up-going and down-going pressure fields at layer 3's top from the recorded data. The red dashed line is the deconvolved result from the forward modeling result. As the forward modeling process is only based on the inverted model, the deconvolved result from

the modelling result coincides with a part of the deconvolution result from the recorded data (red dashed box). By the time-space causality rule, these coincided responses are errors. After eliminating these errors, the first response in Figure 5.5 (b) from the deconvolved result is the response of the first reflector below.

Using the data in Figure 5.3 and following the DWI steps in the previous section, I invert for the velocity profile shown in Figure 5.6:

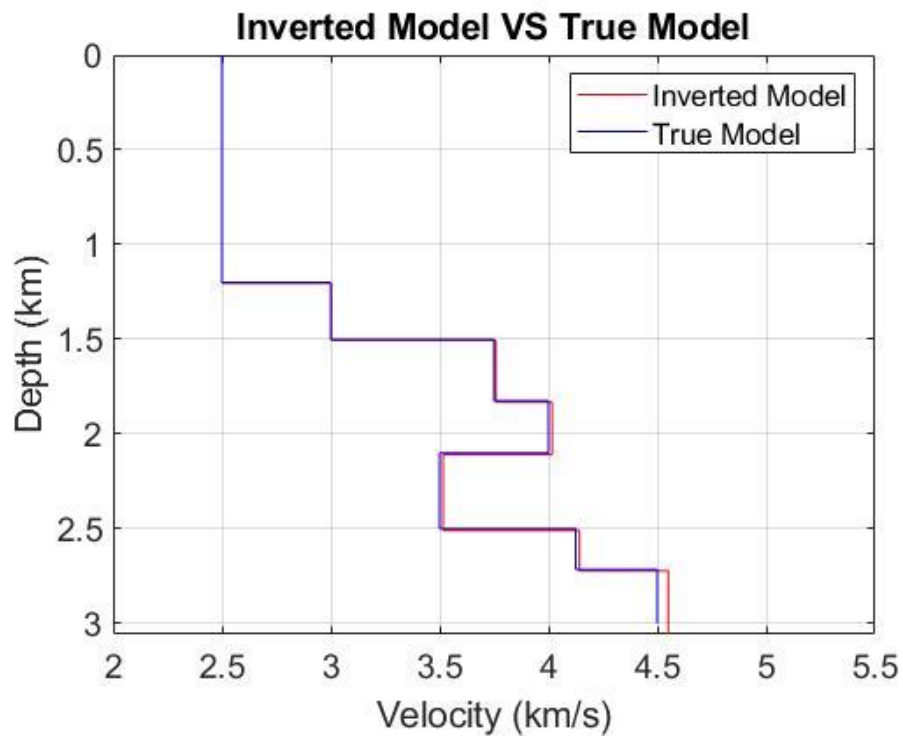


**Figure 5.6:** Comparison between the inversion result (red) and input velocity profile (blue).

Based on the comparison in Figure 5.6, this method provides an excellent inversion recovery of the true velocity profile using only the zero-offset record of the pressure and particle velocity fields.

## **5.4 Discussion and Conclusions**

In this study, I demonstrate a modified 1D DWI scheme able to be applied to the 2D inversion problem. As the 1D scheme could not describe all the propagating behaviors of the spherical wavefields, errors are generated during the inversion process. To overcome this difficulty, I revisit the causality rule of space-time domain wavefields and add additional forward modeling processes into the scheme. Based on the part of the model that is already inverted, the forward modeling result could be used to eliminate the errors and invert the layer's velocities with amplitude errors. A numerical example is also provided to demonstrate the feasibility of this scheme.

Considering the similarity between 2D and 3D wave propagation behaviors, this scheme also has a good potential to be adopted for 3D stratified layered models and to be applied for more practical problems.

## Chapter 6. Relation to the Gelfand-Levitan-Marchenko (GLM) Equation in Geophysical Study

The developments and applications of the Marchenko-type equation have become a very active research area in recent years. As a family of methods based on the 1D direct inversion theory, they have many features that the DWI schemes share. In this Chapter, I first look into the fundamental applications of the Gelfand-Levitan-Marchenko (GLM) equation in geophysics and then provide a numerical test of it. At the end of this chapter, I compare these GLM applications with the DWI methods.

### 6.1 Introduction

The Gelfand-Levitan-Marchenko (GLM) (Agranovich and Marchenko 1963) equation governs a significant part of the scattering theory and plays a significant role throughout the history of the direct inversion study.

From the late 1960s to the early 1980s, the GLM equation was mainly used to solve scattering potentials from the recorded responses. The wave equation was represented in the form of the Schrodinger equation (Ware and Aki 1969, Burridge 1980). The advantage of such inversion schemes is that they do not rely on any *a priori* knowledge of the model. However, as a prerequisite of solving wave equations in the form of the Schrodinger equation, the applications of such inversion schemes were limited to continuous medium to ensure a good recovery of the medium

property. After the early 1980s, the GLM equation did not receive much further interests until 2002. Rose (2002) proposed a “single-sided” auto focusing approach to focus the acoustic wavefield into a layered medium at a certain time while the velocity profile is unknown. In Rose’s study, he also demonstrated the connection between the “single-sided” auto focusing approach and GLM equations through an iterative method. Rose’s work provided a new direction for utilizing the GLM equation. Based on his approach, Wapenaar and his colleagues developed Marchenko-type equations (Slob et al. 2014, Wapenaar et al. 2014, Wapenaar et al. 2014). With the knowledge of the first reflections’ traveltimes above the focusing depth, the Marchenko-type equation can focus seismic wavefields into a heterogeneous medium from receivers by canceling all the internal multiples. Compared with the direct inversion approaches that directly apply the GLM equations, the Marchenko-type equations are not restricted by the smoothness of the medium property. In recent years, Marchenko-type equations were further developed into the Marchenko imaging scheme and received extensive studies and practical applications (Jia et al. 2018, Zhang et al. 2018, van IJsseldijk and Wapenaar 2020).

In this chapter, I first review the GLM equation in geophysics studies, including the transformation from the wave equation to the Schrodinger equation and the GLM equation’s relation to the focusing approaches. Then I present a numerical test on the direct inversion approach based on the GLM equation. In the final part, I provide some discussions, comparing the DWI schemes and the GLM equation applications.

## 6.2 Review of the application of the GLM equation in geophysics studies

### 6.2.1 Applying the GLM equation for the 1D direct inversion

In this section, I review the application of the GLM equation in the 1D direct inversion. In quantum mechanics, by solving the GLM equation

$$K(\zeta, t) = -R(t + \zeta) - \int_{-\zeta}^{\zeta} K(\zeta, \tau) R(\tau + \zeta) d\tau, \quad (6.1)$$

one can retrieve the kernel function  $K(\zeta, t)$  of the whole model based on the observed data  $R$  from one side of the model. Here  $x$  and  $t$  are the space and time coordinate,  $\tau$  is the travelttime represented in relation (6.2)

$$\frac{dx}{d\zeta} = c(x), \quad (6.2)$$

where  $c(x)$  is the velocity of propagation.

Then the scattering potential can be recovered from  $K(\zeta, t)$  by the relation given in (6.3):

$$q(\zeta) = 2dK/d\zeta. \quad (6.3)$$

To adapt the GLM equation to geophysics applications, one has to transform the wave equation to the form of the Schrodinger equation to meet the requirement of

the GLM equation. According to the work by Ware and Aki (1969), start from the elastic wave equation (6.4)

$$\rho(x) \frac{\partial^2 U(x,t)}{\partial t^2} = \frac{\partial}{\partial x} \left[ E(x) \frac{\partial U(x,t)}{\partial x} \right], \quad (6.4)$$

where  $\rho(x)$  is the medium's density,  $U(x,t)$  is the displacement field, and  $E(x)$  is the elastic parameter.

By replacing  $U(x,t)$  with new dependent variable  $\Phi(x,t)$  given in (6.5)

$$\Phi(x,t) = [\rho(x)c(x)]^{\frac{1}{2}} U(x,t), \quad (6.5)$$

equation (6.4) could be represented in the form of the Schrodinger equation by  $\zeta$  and  $t$  in equation (6.6), or by  $\zeta$  and  $\omega$  (frequency domain) in the equation (6.7)

$$\frac{\partial^2 \Phi(\zeta,t)}{\partial \zeta^2} - \frac{\partial^2 \Phi(\zeta,t)}{\partial t^2} = q(\zeta) \Phi(\zeta,t), \quad (6.6)$$

$$\frac{\partial^2 \Phi(\zeta,\omega)}{\partial \zeta^2} + \omega^2 \Phi(\zeta,\omega) = q(\zeta) \Phi(\zeta,\omega). \quad (6.7)$$

In equation (6.6) and (6.7),  $q(\zeta)$  has the form below

$$q(\zeta) = [1/\eta(\zeta)] [d^2\eta(\zeta)/d\zeta^2], \quad (6.8)$$

where

$$\eta(\zeta) = [\rho(\zeta)c(\zeta)]^{\frac{1}{2}}. \quad (6.9)$$

Finally, after every term in (6.4) has been represented, one can use (6.1) and (6.2) again to retrieve the  $q(\zeta)$ , and  $\rho(\zeta)c(\zeta)$  could be recovered through the integrating equation (6.8). For the derivation of the Schrodinger's representation of the acoustic wave equation, every term keeps the same form as elastic wave equations except  $\eta(\zeta)$  becomes the reciprocal form of (6.9)

$$\eta_{\text{acoustic}}(\zeta) = [\rho(\zeta)c(\zeta)]^{-\frac{1}{2}}. \quad (6.10)$$

Note that compared with the original potential calculation process applying the GLM equation on the Schrodinger equation, calculating  $\eta(\zeta)$  from the wave equations involves an extra second-order derivative operation in (6.8). To assure the whole process is well defined, the application of the equation on the wave equations has a much more strict constrain on the continuity of the model's impedance. Recently, Wu (2018) introduced a new method that significantly relieved this issue, which is also pointed out by Berryman and Greene (1980): As the impedance equation observes the zero-frequency Schrodinger equation, it can be solved by the zero-frequency Jost solution of the Schrodinger equation

$$\eta(\zeta) = \eta(0) \left[ 1 + \int_{-\zeta}^{\zeta} K(\zeta, \tau) d\tau \right]. \quad (6.11)$$

## 6.2.2 Applying the GLM equation in the 1D focusing approaches

In this section, I review the application of the GLM equation in the 1D focusing approaches. The term “focusing” here refers to generating new incident waves that cancel all the multiples above the target point, which is demonstrated in an iterative process in the work by Rose (2002).

Consider a step-function velocity profile shown in Figure 6.1.

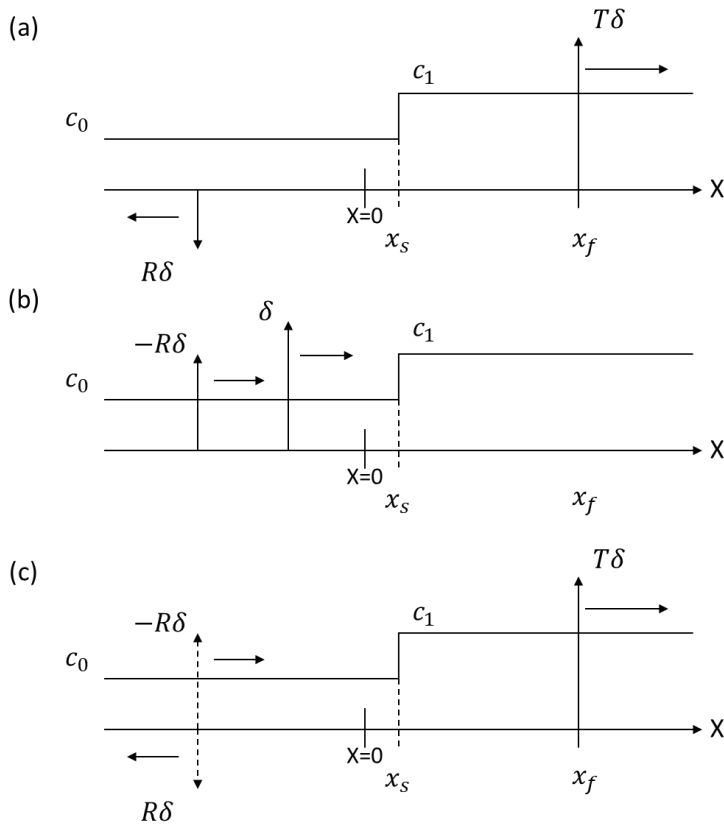


**Figure 6.1:** A step-function velocity profile, the velocity is  $c_0$  to the left of  $x_s$  and  $c_1$  to the right of  $x_s$ .  $R$  is the reflection coefficient and  $T$  is the transmission coefficient. The horizontal arrows show the direction of events’ propagation. (a) The reflected and transmitted pulses due to the delta function. (b) The incident fields focus at  $x_f$ ,

consist of two pulses with strength one and a second impulse with strength -R. (c)

The fields focus at  $x_f$ , the reflected pulse is cancelled by the second incident pulse.

The incident wave could be focused by the following step.

Step 1. Send an incident impulse  $\delta(t - x/c_0 + t_f)$ , where  $t_f$  is the time  $T\delta$  arriving at

$x_f$ .

Step 2. Record the reflected pulse  $R\delta(t + x/c_0 - 2x_s/c_0 + t_f)$ .

Step 3. Evaluate the result at  $x = 0$  and truncate everything that comes back after  $t_f$  to

obtain  $R\delta(t - 2x_s/c_0 + t_f)$ .

Step 4. Time reverse the result to find  $R\delta(t + 2x_s/c_0 - t_f)$ .

Step 5. Subtract the result from the leading delta function to find

$$\delta(t + t_f) - R\delta(t + 2x_s/c_0 - t_f).$$

Step 6. Replace  $t$  by  $t - x/c_0$  to obtain the new incident pulse  $\phi_{in}^{(2)}$

$$\begin{aligned} \phi_{in}^{(2)}(t - x/c_0 : t_f) \\ = \delta(t - x/c_0 + t_f) - R\delta(t - x/c_0 + 2x_s/c_0 + t_f) \end{aligned} \quad (6.12)$$

With the new incident pulse, at  $t = 0$ , the total field  $\phi_{total}^f$  contains only a single delta function

$$\phi_{total}^f(t = 0, x : t_f) = T\delta(x_f/c_1 - x/c_1). \quad (6.13)$$

For a more complicated medium, the process above needs to be iterated until  $\phi_{in}$  converges. The relation of the  $n^{th}$  iteration's incident wavefield  $\phi_{in}^{(n)}$  and the reflected wavefield measured at  $x=0$  and  $\phi_{out}^{(n)}$  is shown in (6.14)

$$\phi_{\text{out}}^{(n)}(t) = \int_{-\infty}^{\infty} dt' R(t-t') \phi_{\text{in}}^{(n)}(t'). \quad (6.14)$$

Based on (6.14), the whole iterative process could be further represented in a series as

(6.15) and (6.16)

$$\begin{aligned} \phi_{\text{out}}^{(n)}(t:t_f) = & R(t+t_f) - \int_{-\infty}^{t_f} dt' R(t+t') R(t'+t_f) \\ & + \int_{-\infty}^{t_f} dt'' \int_{-\infty}^{t_f} dt' R(t+t') R(t'+t'') R(t''+t_f) + \dots \end{aligned} \quad (6.15)$$

$$\phi_{\text{out}}^f(t:t_f) = R(t+t_f) - \int_{-\infty}^{t_f} dt' R(t+t') \phi_{\text{out}}^f(t':t_f), \quad (6.16)$$

The focusing process is equivalent to iterating the GLM equation (6.1), as

(6.15) has the form of the Neumann series, the convergence is guaranteed.

### 6.3 Numerical test

In this section, I go through the reviewed approaches with a numerical test. First, I build a model makes of 500 grids with 3 meters as the size of each grid and has a constant density value equals  $1\text{g/cm}^3$ . The true model's velocity profile is generated by a tapered cosine function shown in Figure 6.2. Both source and receiver are placed at a 400-meter distance. The model's left and right boundaries are both half spaces. I used the 1D finite difference method to generate a synthetic wavefield to prepare for this inversion input. The time interval of recording data is 0.25ms. The source used here is a Ricker wavelet with a central frequency of 15Hz. As the GLM algorithm requires an input of impulse responses, a deconvolution process was applied after forward modeling to generate the input data shown in Figure 6.3.

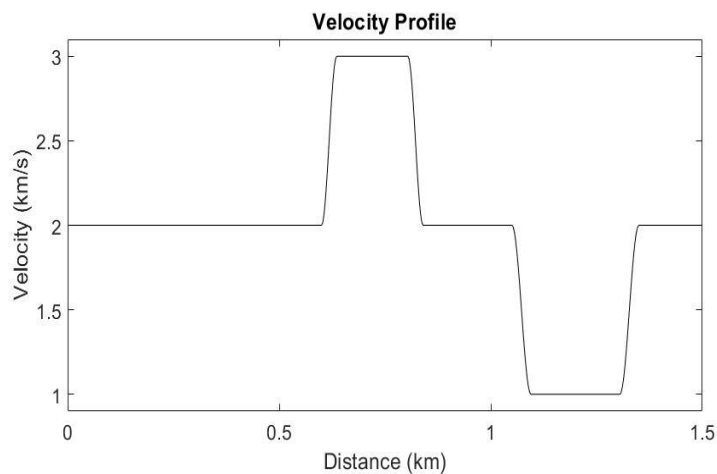


**Figure 6.2:** Velocity profile of the true model. The velocity is generated by the tapered cosine function.

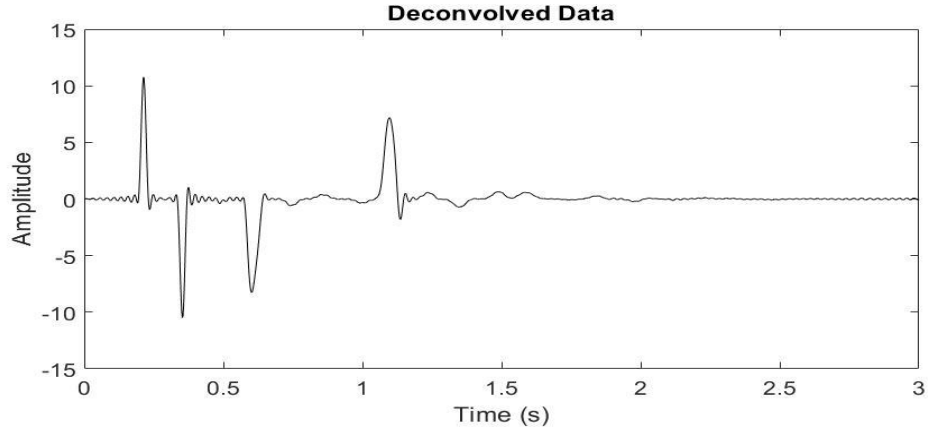


**Figure 6.3:** Deconvolved Data as 1D inversion's input.

To calculate  $K(\zeta, t)$ , I follow the iterative process in (6.16), for the  $n^{th}$  iteration, the equation is written as

$$K_n(\zeta, t) = -R(t + \zeta) - \int_{-\zeta}^{\zeta} K_{n-1}(\zeta, \tau) R(t + \tau) d\tau, \quad (6.17)$$

where I use the deconvolved reflection time series as the initial guess for  $K_0(\zeta, t)$ . In this test  $K(\zeta, t)$  converges after five iterations, the diagonal terms  $K_{diag}$  of matrix  $K$  after first, third, and fifth iterations are shown as time series in Figure 6.4.

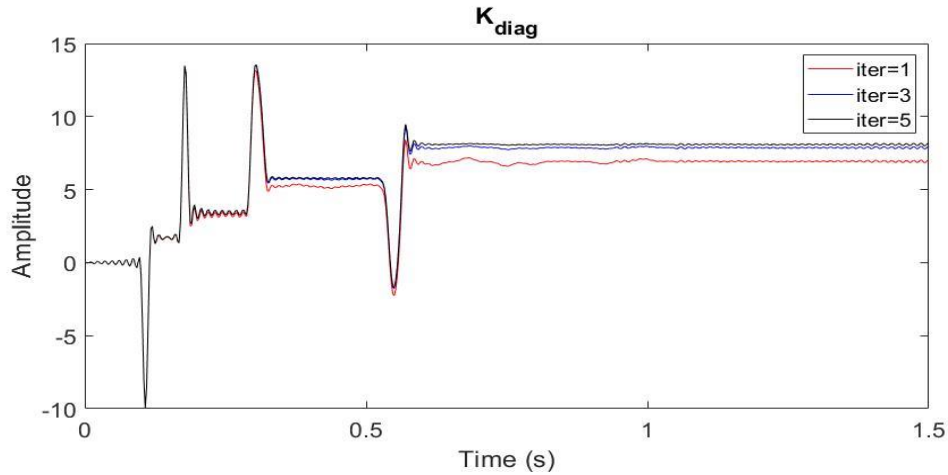


**Figure 6.4:** The diagonal terms  $K_{diag}$  of the kernel function matrix  $K$  after the first iteration (red line), third iteration (blue line), and fifth iteration (black line).

With  $K_{diag}$  I then follow (6.3) to calculate  $q$ , the comparison of  $q$  calculated from the true model and  $K_{diag}$  is shown in Figure 6.5, two results have a good match except for the small artifacts on  $q$  calculated from  $K_{diag}$ . Such artifacts are numerical errors in the deconvolution process, as similar artifacts could also be observed from the input data in Figure 6.3.

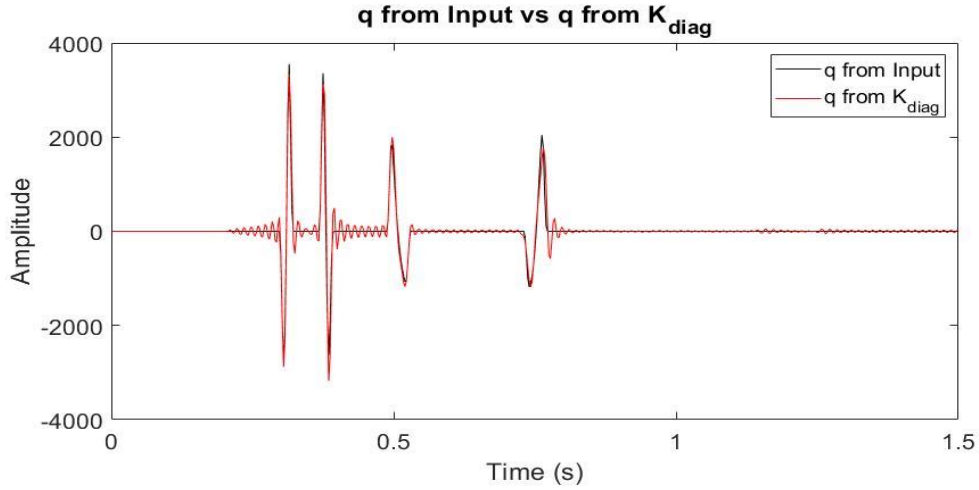


**Figure 6.5:** Time series of scattering potential  $q$  calculated from the true model and  $K_{\text{diag}}$ .

Finally, I use both (6.8) (Ware and Aki 1969) and (6.11) (Wu 2018) to calculate  $\eta_{\text{acoustic}}$  then use (6.10) for velocity (impedance) profiles' reconstruction. To solve (6.8), a four points Runge-Kutta method is applied. The time series of the velocity profiles from inversion results and the initial model are presented below (Figure 6.6).

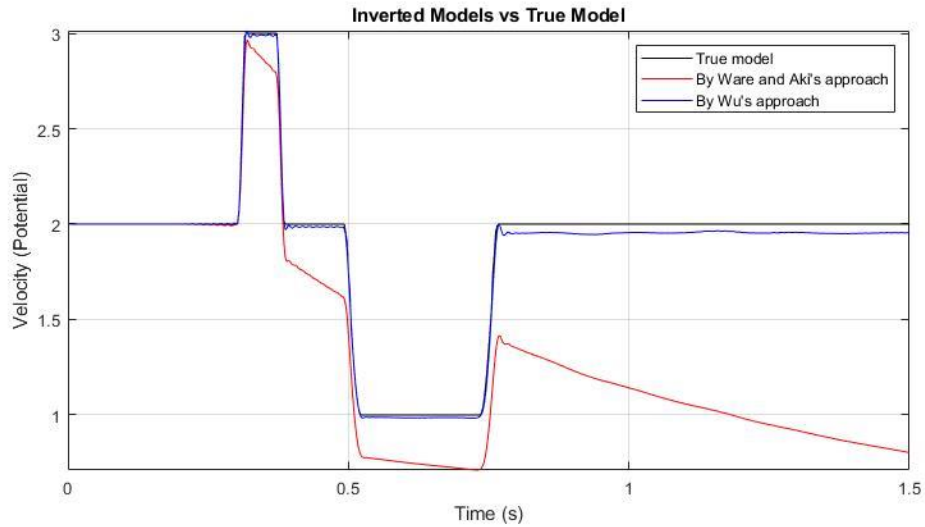


**Figure 6.6:** Comparison of the Inversion results calculated from  $q$ ,  $K$  and the true model.

In Figure 6.6, the velocity profile recovered from  $q$  has a very bad matching with the true model. As discussed in section 6.2.1, such calculation process is strictly relying on the continuity of the model's properties, the tapered cosine functions used to initialize the true model might not meet the continuity requirement and result in the breaking down of the equation (6.8) (red line). On the contrary, the result from equation (6.11) (blue line) does not suffer from the discontinuity issue and has a very satisfying accuracy.

## 6.4 Discussions

Compare with the inversion schemes based on the model matching approaches, the direct inversion with the GLM equation has the advantage of only relying on the observation from one side of the model to reconstruct the whole model. Moreover, by representing the wave equation with the Schrodinger equation, the model could be reconstructed more straightly through calculating the GLM equation than other direct inversion methods replying on solving different types of series. With the work by Wu (2018), the GLM inversion further breaks the constrain of requiring a continuous model. As another important application of the GLM equation, the wavefield focusing scheme with the GLM equation aims to reconstruct wavefield at any point inside the medium. Unlike the seismic interferometry methods, the wavefield focusing scheme does not need to put any receiver at the focusing point, and the detailed medium parameters are not required. Instead, only the travelttime of the direct arrival to the focus point is needed for retrieving the Green's function.

For the advantages of the GLM equation's applications discussed above, many can also be founded in the DWI schemes: By exploiting space-time causality, the DWI can build the model without the information inside the model. Furthermore, the transformation from a global inversion problem to many localized inversion problems by the DWI scheme turns the inversion into a recursive process. In each recursion, as the extrapolated up-going and down-going wavefields are also free from internal multiples from between inversion point and receivers, they could serve for similar purposes as focused wavefields.

Finally, compared with the DWI scheme, one disadvantage of the inversion using the GLM equation is that the velocity profile is output as a time series. Thus, a transformation to the space domain is required for recovering the model. In 1D problems, the transformation could be conducted after the velocity time series is acquired; however, a prior velocity model will be needed for a higher dimensional problem. In contrast, for the DWI schemes, although a mapping process and model information are required, the causality characteristic of the DWI schemes makes it only uses the inverted part of the model.

## **6.5 Conclusions**

I reviewed two applications of the GLM equation in geophysics studies, including 1D direct inversion and wavefield focusing. Then, in the numerical example, I applied the GLM equation for 1D direct inversion and compared the results from different approaches. In the final part, I discussed these applications and some comparisons to the DWI scheme.

## Bibliography

- Agranovich, Z. and V. A. Marchenko (1963). "The inverse problem of scattering theory."
- Agranovich, Z. and V. A. Marchenko (2020). *The inverse problem of scattering theory*, Courier Dover Publications.
- Alkhalifah, T. and R.-É. Plessix (2014). "A recipe for practical full-waveform inversion in anisotropic media: An analytical parameter resolution study." *Geophysics* **79**(3): R91-R101.
- Amundsen, L. (1993). "Wavenumber-based filtering of marine point-source data." *Geophysics* **58**(9): 1335-1348.
- Amundsen, L., B. G. Secest and B. J. G. Arntsen (1995). "Extraction of the normal component of the particle velocity from marine pressure data." *Geophysics* **60**(1): 212-222.
- Backus, M. M. (1959). "Water reverberations—their nature and elimination." *Geophysics* **24**(2): 233-261.
- Baysal, E., D. D. Kosloff and J. W. J. G. Sherwood (1983). "Reverse time migration." *Geophysics* **48**(11): 1514-1524.
- Berryman, J. G. and R. R. Greene (1980). "Discrete inverse methods for elastic waves in layered media." *Geophysics* **45**(2): 213-233.
- Bourgeois, A., B. Jiang and P. Lailly (1989). "Linearized inversion: A significant step beyond pre-stack migration." *Geophysical Journal International* **99**(2): 435-445.
- Bourgeois, A., B. F. Jiang and P. Lailly (1989). "Linearized inversion: a significant step beyond pre-stack migration." *Geophysical Journal International* **99**(2): 435-445.
- Bozdağ, E., J. Trampert and J. Tromp (2011). "Misfit functions for full waveform inversion based on instantaneous phase and envelope measurements." *Geophysical Journal International* **185**(2): 845-870.
- Brossier, R., S. Operto and J. Virieux (2009). "Seismic imaging of complex onshore structures by 2D elastic frequency-domain full-waveform inversion." *Geophysics* **74**(6): WCC105-WCC118.
- Bunks, C., F. M. Saleck, S. Zaleski and G. Chavent (1995). "Multiscale seismic waveform inversion." *Geophysics* **60**(5): 1457-1473.
- Burridge, R. (1980). "The Gelfand-Levitan, the Marchenko, and the Gopinath-Sondhi integral equations of inverse scattering theory, regarded in the context of inverse impulse-response problems." *Wave Motion* **2**(4): 305-323.
- Chen, G. X., R. S. Wu and S. C. Chen (2018). "Reflection multi-scale envelope inversion." *Geophysical Prospecting* **66**(7): 1258-1271.

- Claerbout, J. F. (1976). *Fundamentals of geophysical data processing*, Citeseer.
- Coen, S. (1981). "Density and compressibility profiles of a layered acoustic medium from precritical incidence data." *Geophysics* **46**(9): 1244-1246.
- Coen, S. (1981). "On the elastic profiles of a layered medium from reflection data. Part I. Plane-wave sources." *The journal of the Acoustical Society of America* **70**(1): 172-175.
- Coen, S. (1981). "On the elastic profiles of a layered medium from reflection data. Part II: Impulsive point source." *The journal of the Acoustical Society of America* **70**(5): 1473-1479.
- Eftekhari, R., H. Hu and Y. Zheng (2018). "Convergence acceleration in scattering series and seismic waveform inversion using nonlinear Shanks transformation." *Geophysical Journal International* **214**(3): 1732-1743.
- Eftekhari, R., H. Hu and Y. J. G. J. I. Zheng (2018). "Convergence acceleration in scattering series and seismic waveform inversion using nonlinear Shanks transformation." *Geophysical Journal International* **214**(3): 1732-1743.
- Gauthier, O., J. Virieux and A. Tarantola (1986). "Two-dimensional nonlinear inversion of seismic waveforms - numerical results." *Geophysics* **51**(7): 1387-1403.
- Gauthier, O., J. Virieux and A. Tarantola (1986). "Two-dimensional nonlinear inversion of seismic waveforms: Numerical results." *Geophysics* **51**(7): 1387-1403.
- Ge, Z. and X. Chen (2008). "An efficient approach for simulating wave propagation with the boundary element method in multilayered media with irregular interfaces." *Bulletin of the Seismological Society of America* **98**(6): 3007-3016.
- Goupillaud, P. L. (1961). "An approach to inverse filtering of near-surface layer effects from seismic records." *Geophysics* **26**(6): 754-760.
- Goupillaud, P. L. (1961). "An approach to inverse filtering of near-surface layer effects from seismic records." *Geophysics* **26**: 754-759.
- Ha, W. and C. Shin (2013). "Why do Laplace-domain waveform inversions yield long-wavelength results?" *Geophysics* **78**(4): R167-R173.
- Jeong, W., H.-Y. Lee and D.-J. Min (2012). "Full waveform inversion strategy for density in the frequency domain." *Geophysical Journal International* **188**(3): 1221-1242.
- Jia, X., A. Guitton and R. Snieder (2018). "A practical implementation of subsalt Marchenko imaging with a Gulf of Mexico data set." *Geophysics* **83**(5): S409-S419.
- Kim, Y., C. Shin, H. Calandra and D.-J. Min (2013). "An algorithm for 3D acoustic time-Laplace-Fourier-

domain hybrid full waveform inversion." *Geophysics* **78**(4): R151-R166.

Kolb, P., F. Collino and P. Lailly (1986). "Pre-stack inversion of a 1-D medium." *Proceedings of the IEEE* **74**(3): 498-508.

Lailly, P. (1983). as a Sequence of Before Stack Migrations. Conference on Inverse Scattering--Theory and Application, Siam.

Lailly, P. (1983). The Seismic Inverse Problem as a Sequence of Before-Stack Migrations. Conference on Inverse Scattering: Theory and Applications, SIAM, SIAM, Philadelphia 206-220.

Li, Y. E. and L. Demanet (2016). "Full-waveform inversion with extrapolated low-frequency data." *Geophysics* **81**(6): R339-R348.

Liao, Q. and G. A. McMechan (1996). "Multifrequency viscoacoustic modeling and inversion." *Geophysics* **61**(5): 1371-1378.

Liu, Y., B. He, H. Lu, Z. Zhang, X.-B. Xie and Y. Zheng (2018). "Full-intensity waveform inversion." *Geophysics* **83**(6): R649-R658.

Liu, Y., B. He, H. Lu, Z. Zhang, X. Xie and Y. Zheng (2018). "Full intensity waveform inversion." *Geophysics* **86**(6): R649-R658.

Liu, Y., B. He, Z. Zhang, Y. Zheng and P. Li (2020). "Reflection intensity waveform inversion." *Geophysics* **85**(3): R263-R273.

Liu, Z. and Y. Zheng (2015). Direct waveform inversion. SEG Technical Program Expanded Abstracts 2015, Society of Exploration Geophysicists: 1268-1273.

Liu, Z. and Y. Zheng (2017). Applications of the direct-waveform inversion on 2D models. SEG Technical Program Expanded Abstracts 2017, Society of Exploration Geophysicists: 1687-1691.

Luo, J. and R. S. Wu (2015). "Seismic envelope inversion: reduction of local minima and noise resistance." *Geophysical Prospecting* **63**(3): 597-614.

Mora, P. (1987). "Nonlinear two-dimensional elastic inversion of multioffset seismic data." *Geophysics* **52**(9): 1211-1228.

Mora, P. (1989). "Inversion= migration+ tomography." *Geophysics* **54**(12): 1575-1586.

Mora, P. J. G. (1987). "Nonlinear two-dimensional elastic inversion of multioffset seismic data." *Geophysics* **52**(9): 1211-1228.

Moses, H. (1956). "Calculation of scattering potential from reflection coefficients." *Physical Review*.

Pratt, R. G. (1999). "Seismic waveform inversion in the frequency domain; Part 1, Theory and verification

in a physical scale model." *Geophysics* **64**(3): 888-901.

Pratt, R. G. (2008). Waveform tomography-successes, cautionary tales, and future directions. 70th EAGE Conference and Exhibition-Workshops and Fieldtrips, European Association of Geoscientists & Engineers.

Pratt, R. G., C. Shin and G. J. G. J. I. Hick (1998). "Gauss-Newton and full Newton methods in frequency-space seismic waveform inversion." *Geophysical Journal International* **133**(2): 341-362.

Pratt, R. G. and R. M. J. G. Shipp (1999). "Seismic waveform inversion in the frequency domain, Part 2: Fault delineation in sediments using crosshole data." *Geophysics* **64**(3): 902-914.

Prosser, R. T. (1982). "Formal solutions of inverse scattering problems. IV. Error estimates." *Journal of Mathematical Physics* **23**(11): 2127-2130.

Prosser, R. T. J. J. o. M. P. (1969). "Formal solutions of inverse scattering problems." *Journal of Mathematical Physics* **10**(10): 1819-1822.

Prosser, R. T. J. J. o. M. P. (1976). "Formal solutions of inverse scattering problems. II." *Journal of Mathematical Physics* **17**(10): 1775-1779.

Prosser, R. T. J. J. o. M. P. (1980). "Formal solutions of inverse scattering problems. III." *Journal of Mathematical Physics* **21**(11): 2648-2653.

Razavy, M. (1975). "Determination of the wave velocity in an inhomogeneous medium from the reflection coefficient." *The journal of the Acoustical Society of America* **58**(5): 956-963.

Richardson, A. (2018). "Seismic full-waveform inversion using deep learning tools and techniques."

Rose, J. H. (2002). "'Single-sided' autofocusing of sound in layered materials." *Inverse problems* **18**(6): 1923.

Sams, W. N. and D. J. Kouri (1969). "Noniterative solutions of integral equations for scattering. I. Single channels." *The Journal of Chemical Physics* **51**(11): 4809-4814.

Sears, T. J., S. Singh and P. Barton (2008). "Elastic full waveform inversion of multi-component OBC seismic data." *Geophysical Prospecting* **56**(6): 843-862.

Shin, C. and Y. H. Cha (2008). "Waveform inversion in the Laplace domain." *Geophysical Journal International* **173**(3): 922-931.

Shin, C. and W. Ha (2008). "A comparison between the behavior of objective functions for waveform inversion in the frequency and Laplace domains." *Geophysics* **73**(5): VE119-VE133.

Sirgue, L. and R. G. Pratt (2004). "Efficient waveform inversion and imaging: A strategy for selecting temporal frequencies." *Geophysics* **69**(1): 231-248.

- Slob, E., K. Wapenaar, F. Broggin and R. Snieder (2014). "Seismic reflector imaging using internal multiples with Marchenko-type equations." *Geophysics* **79**(2): S63-S76.
- Tao, Y. and M. K. J. G. Sen (2013). "Frequency-domain full waveform inversion with plane-wave data." *Geophysics* **78**(1): R13-R23.
- Tarantola, A. (1984). "Inversion of seismic-reflection data in the acoustic approximation." *Geophysics* **49**(8): 1259-1266.
- Tarantola, A. (1986). "A strategy for nonlinear elastic inversion of seismic-reflection data." *Geophysics* **51**(10): 1893-1903.
- Tarantola, A. (1986). "A strategy for nonlinear elastic inversion of seismic reflection data." *Geophysics* **51**(10): 1893-1903.
- Tarantola, A. (2005). *Inverse problem theory and methods for model parameter estimation*, SIAM.
- Tarantola, A. J. G. (1984). "Inversion of seismic reflection data in the acoustic approximation." *Geophysics* **49**(8): 1259-1266.
- van IJsseldijk, J. and K. Wapenaar (2020). "Adaptation of the iterative Marchenko scheme for imperfectly sampled data."
- Van Leeuwen, T. and W. Mulder (2008). "Velocity analysis based on data correlation." *Geophysical Prospecting* **56**(6): 791-803.
- Virieux, J. and S. Operto (2009). "An overview of full-waveform inversion in exploration geophysics." *Geophysics* **74**(6): WCC1-WCC26.
- Wang, B., M. Jakobsen, R.-S. Wu, W. Lu and X. J. I. p. Chen (2017). "Accurate and efficient velocity estimation using Transmission matrix formalism based on the domain decomposition method." *Inverse Problems* **33**(3): 035002.
- Wang, Y., R.-S. Wu, G. Chen and Z. Peng (2018). "Seismic modulation model and envelope inversion with smoothed apparent polarity." *Journal of Geophysics and Engineering* **15**(5): 2278-2286.
- Wapenaar, K., J. Thorbecke, J. van der Neut, F. Broggin, E. Slob and R. Snieder (2014). "Green's function retrieval from reflection data, in absence of a receiver at the virtual source position." *The journal of the Acoustical Society of America* **135**(5): 2847-2861.
- Wapenaar, K., J. Thorbecke, J. Van Der Neut, F. Broggin, E. Slob and R. J. G. Snieder (2014). "Marchenko imaging." *Geophysics* **79**(3): WA39-WA57.
- Ware, J. A. and K. Aki (1969). "Continuous and discrete inverse-scattering problems in a stratified elastic medium. I. Plane waves at normal incidence." *The journal of the Acoustical Society of America* **45**(4): 911-921.

Warner, M., A. Ratcliffe, T. Nangoo, J. Morgan, A. Umpleby, N. Shah, V. Vinje, I. Štekl, L. Guasch and C. Win (2013). "Anisotropic 3D full-waveform inversion." *Geophysics* **78**(2): R59-R80.

Weglein, A., K. Matson, D. Foster, P. Carvalho, D. Corrigan and S. Shaw (2000). Imaging and inversion at depth without a velocity model: Theory, concepts and initial evaluation. SEG Technical Program Expanded Abstracts 2000, Society of Exploration Geophysicists: 1016-1019.

Weglein, A. B., F. V. Araújo, P. M. Carvalho, R. H. Stolt, K. H. Matson, R. T. Coates, D. Corrigan, D. J. Foster, S. A. Shaw and H. Zhang (2003). "Inverse scattering series and seismic exploration." *Inverse Problems* **19**(6): R27.

Weglein, A. B., D. J. Foster, K. H. Matson, S. A. Shaw, P. M. Carvalho and D. Corrigan (2001). An inverse-scattering sub-series for predicting the spatial location of reflectors without the precise reference medium and wave velocity. SEG Technical Program Expanded Abstracts 2001, Society of Exploration Geophysicists: 2108-2111.

Weglein, A. B., F. A. Gasparotto, P. M. Carvalho and R. H. J. G. Stolt (1997). "An inverse-scattering series method for attenuating multiples in seismic reflection data." *Geophysics* **62**(6): 1975-1989.

Wu, R.-S. (2018). Direct envelope inversion and the inverse problem of Schrodinger impedance equation. SEG Technical Program Expanded Abstracts 2018, Society of Exploration Geophysicists: 1188-1192.

Wu, R.-S., J. Luo and B. Wu (2013). Ultra-low-frequency information in seismic data and envelope inversion. SEG Technical Program Expanded Abstracts 2013, Society of Exploration Geophysicists: 3078-3082.

Wu, R.-S., J. Luo and B. Wu (2014). "Seismic envelope inversion and modulation signal model." *Geophysics* **79**(3): WA13-WA24.

Wu, R.-S. and Y. Zheng (2014). "Non-linear partial derivative and its De Wolf approximation for non-linear seismic inversion." *Geophysical Journal International* **196**(3): 1827-1843.

Wu, R. and H. He (2020). Inverse Scattering for Schrödinger Impedance Equation and Simultaneous p-v Inversion in Layered Media. 82nd EAGE Annual Conference & Exhibition, European Association of Geoscientists & Engineers.

Xie, X.-B. (2013). Recover certain low-frequency information for full waveform inversion. SEG Technical Program Expanded Abstracts 2013, Society of Exploration Geophysicists: 1053-1057.

Yao, J., A.-C. Lesage, B. G. Bodmann, F. Hussain and D. J. Kouri (2014). "One dimensional acoustic direct nonlinear inversion using the Volterra inverse scattering series." *Inverse problems* **30**(7): 075006.

Zhang, L., E. Slob, J. van der Neut and K. Wapenaar (2018). "Artifact-free reverse time migration." *Geophysics* **83**(5): A65-A68.

Zheng, Y. (2010). "Retrieving the exact Green's function by wavefield crosscorrelation." The journal of the Acoustical Society of America **127**(3): EL93-EL98.

Zheng, Y. and Z. Liu (2020). "Concepts in the Direct Waveform Inversion (DWI) Using Explicit Time-Space Causality." COMMUNICATIONS IN COMPUTATIONAL PHYSICS **28**(1): 342-355.

Zhou, H.-W. (2014). Practical seismic data analysis, Cambridge University Press.